



## **MeerKAT view of Hickson Compact Groups II. Hi deficiency in the cores and surrounding regions**

Downloaded from: <https://research.chalmers.se>, 2025-06-16 18:29 UTC

Citation for the original published paper (version of record):

Sorgho, A., Verdes-Montenegro, L., Ianjamasimanana, R. et al (2025). MeerKAT view of Hickson Compact Groups II. Hi deficiency in the cores and surrounding regions. *Astronomy and Astrophysics*, 696. <http://dx.doi.org/10.1051/0004-6361/202452995>

N.B. When citing this work, cite the original published paper.

# MeerKAT view of Hickson Compact Groups

## II. HI deficiency in the cores and surrounding regions

A. Sorgho<sup>1,\*</sup>, L. Verdes-Montenegro<sup>1</sup>, R. Ianjamasimanana<sup>1</sup>, K. M. Hess<sup>2,3,1</sup>, M. G. Jones<sup>4</sup>, M. Korsaga<sup>5,1</sup>,  
 J. Wang<sup>6</sup>, X. Lin<sup>7</sup>, J. M. Solanes<sup>8,9</sup>, M. E. Cluver<sup>10</sup>, J. M. Cannon<sup>11</sup>, A. Bosma<sup>12</sup>, E. Athanassoula<sup>12</sup>,  
 A. del Olmo<sup>1</sup>, J. Perea<sup>1</sup>, J. Moldón<sup>1</sup>, T. Wiegert<sup>1</sup>, S. Sanchez-Expósito<sup>1</sup>, J. Garrido<sup>1</sup>, R. García-Benito<sup>1</sup>,  
 G. I. G. Józsa<sup>13,14</sup>, S. Borthakur<sup>15</sup>, T. Jarrett<sup>16,17</sup>, B. Namumba<sup>1</sup>, E. Pérez<sup>1</sup>, J. Román<sup>18</sup>,  
 O. M. Smirnov<sup>19,20,21</sup>, and M. Yun<sup>22</sup>

<sup>1</sup> Instituto de Astrofísica de Andalucía (CSIC), Glorieta de la Astronomía s/n, 18008 Granada, Spain

<sup>2</sup> Department of Space, Earth and Environment, Chalmers University of Technology, Onsala Space Observatory, 43992 Onsala, Sweden

<sup>3</sup> Netherlands Institute for Radio Astronomy (ASTRON), Postbus 2, 7990 AA Dwingeloo, The Netherlands

<sup>4</sup> Steward Observatory, University of Arizona, 933 North Cherry Avenue, Rm. N204, Tucson, AZ 85721-0065, USA

<sup>5</sup> Laboratoire de Physique et de Chimie de l'Environnement, Université Joseph Ki-Zerbo, 03 BP 7021, Ouaga 03, Burkina Faso

<sup>6</sup> Kavli Institute for Astronomy and Astrophysics, Peking University, Beijing 100871, PR China

<sup>7</sup> Department of Astronomy, School of Physics, Peking University, Beijing 100871, PR China

<sup>8</sup> Departament de Física Quàntica i Astrofísica, Universitat de Barcelona, C. Martí i Franquès 1, 08028 Barcelona, Spain

<sup>9</sup> Institut de Ciències del Cosmos (ICCUB), Universitat de Barcelona, C. Martí i Franquès 1, 08028 Barcelona, Spain

<sup>10</sup> Centre for Astrophysics and Supercomputing, Swinburne University of Technology, Hawthorn, VIC 3122, Australia

<sup>11</sup> Department of Physics & Astronomy, Macalester College, 1600 Grand Avenue, Saint Paul, MN 55105, USA

<sup>12</sup> Aix Marseille Univ, CNRS, CNES, LAM, Marseille, France

<sup>13</sup> Max-Planck-Institut für Radioastronomie, Auf dem Hügel 69, 53121 Bonn, Germany

<sup>14</sup> Department of Physics and Electronics, Rhodes University, PO Box 94, Makhanda 6140, South Africa

<sup>15</sup> School of Earth and Space Exploration, Arizona State University, 781 Terrace Mall, Tempe, AZ 85287, USA

<sup>16</sup> Astronomy Department, University of Cape Town, Private Bag X3, Rondebosch 7701, South Africa

<sup>17</sup> Inter-University Institute for Data Intensive Astronomy (IDIA), University of Cape Town, Rondebosch, Cape Town 7701, South Africa

<sup>18</sup> Departamento de Física de la Tierra y Astrofísica, Universidad Complutense de Madrid, E-28040 Madrid, Spain

<sup>19</sup> Centre for Radio Astronomy Techniques and Technologies (RATT), Department of Physics and Electronics, Rhodes University, Makhanda 6140, South Africa

<sup>20</sup> South African Radio Astronomy Observatory, Black River Park, 2 Fir Street, Observatory, Cape Town 7925, South Africa

<sup>21</sup> Institute for Radioastronomy, National Institute of Astrophysics (INAF IRA), Via Gobetti 101, 40129 Bologna, Italy

<sup>22</sup> Department of Astronomy, University of Massachusetts, Amherst, MA 01003, USA

Received 14 November 2024 / Accepted 5 March 2025

### ABSTRACT

**Context.** Hickson compact groups (HCGs) offer an ideal environment for investigating galaxy transformation as a result of interactions. It has been established that the evolutionary sequence of HCGs is marked by an intermediate stage characterised by a substantial amount of HI in their intragroup medium (IGrM) in the form of tidal tails and bridges (phase 2), rapidly followed by a final stage in which no IGrM gas is found and in which their member galaxies are highly HI deficient (phase 3).

**Aims.** Despite numerous single-dish and interferometric HI studies on the HCGs, a clear HI picture of the groups within their large-scale environment still remains to be uncovered. Taking advantage of MeerKAT's high column density sensitivity and large field of view, we aim to investigate the rapid transformation of HCGs from the intermediate to late phases, and establish a picture of their gas content variations in the context of their large-scale environments.

**Methods.** We performed MeerKAT observations of six HCGs that were selected to represent the intermediate and late phases of the proposed evolutionary sequence. Combining the HI observations with data from recent wide-field optical surveys, we evaluated the HI deficiencies of galaxies in a  $\sim 30'$  radius of the HCGs.

**Results.** We find that galaxies surrounding both phases exhibit similar distributions in their gas content. Similarly, galaxies making up the cores of phase 2 HCGs are comparable to their neighbours in terms of HI deficiencies. However, phase 3 groups are over an order of magnitude more deficient than their surroundings, supporting previous findings that late-phase HCG galaxies are more evolved than their large-scale environments.

**Key words.** galaxies: evolution – galaxies: interactions – intergalactic medium

\* Corresponding author; [asorgho@iaa.es](mailto:asorgho@iaa.es)

## 1. Introduction

Standard models of structure formation predict that individual galaxies assemble hierarchically to form larger structures such as groups and clusters in the Universe (e.g. [White & Rees 1978](#); [Blumenthal et al. 1984](#); [Springel et al. 2005](#)). Observations of galaxies in environments with different densities have revealed a systematic difference in morphological distributions, with dense environments predominantly populated by early-type, gas-deficient galaxies, and the late-type, gas-rich galaxies tending to reside in low-density environments ([Dressler 1980](#); [Goto et al. 2003](#)). It is believed that galaxies undergo gas-stripping mechanisms when they fall within high-density structures, such as clusters ([Gunn & Gott 1972](#); [Cayatte et al. 1990](#); [Vollmer et al. 2001](#); [Ramatsoku et al. 2019, 2020](#); [Moretti et al. 2023](#)). More recent studies have shown that a significant part of these gas removal processes, a phase known as pre-processing, takes place inside galaxy groups (e.g. [Hess & Wilcots 2013](#); [Bahé et al. 2013](#); [Jones et al. 2020](#)). The most well-studied cases of gas stripping processes include substructures within the Virgo cluster (e.g. [Kenney et al. 2004](#); [Chung et al. 2007](#); [Sorgho et al. 2017](#)) and within the Hydra cluster (e.g. [Hess et al. 2022](#)). Similar processes have also been observed in group environments within other nearby clusters (e.g. [Džudžar et al. 2019](#); [Healy et al. 2021](#)) where the effects of these mechanisms on the HI content have been demonstrated. This makes galaxy groups ideal places to investigate processes affecting galaxy properties that may lead to their transformation throughout their lifetime.

A type of galaxy aggregation that deserves particular interest is compact groups, namely the Hickson Compact Groups ([Hickson 1982](#), HCGs;). These are collections of four to ten galaxies distributed in compact configurations and located in low-density environments, often showing signs of extreme gravitational interactions. They present low velocity dispersions, typically  $\lesssim 200 \text{ km s}^{-1}$  ([Hickson et al. 1992](#)). Due to their compactness, HCGs represent unique laboratories in which to study the effects of repeated tidal encounters and the role of intragroup gas on galaxy evolution.

Various HI studies have found that several of the catalogued HCGs are HI deficient ([Huchtmeier 1997](#); [Verdes-Montenegro et al. 2001](#); [Williams et al. 2002](#)), presumably because they have lost a significant fraction of their cold gas reservoir throughout their evolution. In the first large study of the HI content of HCGs, [Verdes-Montenegro et al. \(2001\)](#) studied 72 HCGs, of which 16 were imaged at high resolution with the Very Large Array (VLA) telescope and the remaining with single-dish telescopes. The authors proposed an evolutionary sequence of HCGs with four phases: phase 1, in which the HI distribution and kinematics are unperturbed and  $\geq 90\%$  of gas is in the discs of the galaxy members, phase 2, in which 30–60% of the gas is in the form of tidal features, and phase 3a, in which most of the HI is stripped from the disc and is either found in tails or altogether missing. Furthermore, an additional and uncommon phase 3b consists of a stage where the essential part of the HI in the group core is contained in large HI clouds with a single velocity gradient. Later, [Borthakur et al. \(2010\)](#) performed deep single-dish GBT observations of 22 HCGs covering all three main phases, measuring an average mass of  $8 \times 10^9 M_{\odot}$  per group. In a comparative study with interferometric VLA data compiled from various sources, the authors recovered excess HI (with respect to VLA-measured masses) in all HCGs. They particularly found that the highest fraction of excess gas was observed in phase 2 groups, with an average excess-to-measured-mass fraction of 48%. The most

recent study on the subject, [Jones et al. \(2023\)](#), followed up on these investigations by reprocessing VLA data of 38 HCGs and found that phase 1 and 2 have consistent HI deficiencies. However, phase 3 groups are found to be much more deficient, with 90% of their gas missing. They also identified a new phase 3c characterised by a single HI-bearing galaxy in an otherwise highly HI-deficient group, likely the result of an evolved group acquiring a new gas-rich member. However, due to the limited column density sensitivity of interferometers, it is unclear whether the cores of the late-phase HCGs studied in [Jones et al. \(2023\)](#) are indeed HI-deficient or, in fact, contain an amount of HI in a diffuse form that is not revealed by these observations. The environmental mechanisms responsible for gas depletion in group galaxies can be categorised into two types: tidal interactions between a galaxy and its neighbours, and interactions with the intragroup medium (IGrM). While evidence is found for both types of interactions in HCGs, several studies reveal that a significant fraction of compact groups lack prominent X-ray emission, a tracer of the hot gas in the IGrM. In those groups, either no diffuse hot gas is detected, or it is linked to individual galaxies (e.g. [Rasmussen et al. 2008](#); [Desjardins et al. 2013](#)). Furthermore, [Desjardins et al. \(2014\)](#) found that high luminosity X-ray emission tends to be associated with high baryonic mass compact groups, while those of lower masses are observed to host localised X-ray emission. The study further found that the most X-ray luminous groups experience the lowest star formation rates (SFRs), argued to be the consequence of the lack of cold gas to form stars. However, the X-ray luminosity is not correlated with the HI deficiency of the groups, such that not all gas-deficient HCGs are X-ray luminous and vice versa. This favours the argument that galaxy-IGrM interactions are not the dominant processes responsible for HI removal from galaxies in the cores of HCGs ([Rasmussen et al. 2008](#)), although they remain important (e.g. [Deb et al. 2023](#)). This highlights the important role of tidal interactions in the observed HI deficiency of HCG cores. It is believed that these galaxy-galaxy interactions, more frequent in the past, have transformed the cores of the groups into evolved systems that are embedded into more extended structures evolving more slowly ([Coziol et al. 1998](#)). This picture is supported by the more recent analysis of the molecular gas in galaxies selected in 12 HCGs, revealing that the most evolved galaxies in these systems experience the most severe star formation suppression, caused by a disruption of the existing molecular gas in the group ([Alatalo et al. 2015](#)).

Thanks to the upgraded capabilities of the MeerKAT telescope, a more complete HI map of six HCGs selected in phases 2 and 3 has recently become available ([Ianjamasimanana et al. 2025](#)). In this work, we present a detailed HI deficiency study of galaxy members of these HCG groups. In particular, we examine the distribution of the deficiency in the groups and their immediate surrounding, and investigate any link between the groups and their environment in terms of gas depletion. Through this study, we aim to understand how HCGs transition from an impressive complex of HI tidal structures and diffuse gas to an evolved state in which galaxies have completely lost their HI. Furthermore, we aim to uncover the full picture of the effects of the rapid transformation on the gas content of galaxies in the larger scale HCGs environments.

The paper is organised as follows. In Sect. 2 we describe the sample and the HI observations. In Sect. 3 we detail the procedures followed to measure the optical photometry of the galaxies in the HCG environments and determine their stellar masses.

**Table 1.** Properties of the HCGs.

Phase	HCG	RA	Dec	$V_{\text{sys}}$	$\sigma_v$	Dist.	$M_{\text{vir}}$	$r_{\text{vir}}$	N
(1)	(2)	(J2000)	(3)	(km s <sup>-1</sup> )	(km s <sup>-1</sup> )	(Mpc)	(10 <sup>12</sup> M <sub>⊙</sub> )	(kpc)	(9)
2	16	02:09:31.97	-10:09:25.67	3977	98.9	49	2.2 ± 1.8	268.8 ± 73.7	5
	31	05:01:39.27	-04:15:45.63	4068	50.1	53	0.1 ± 0.1	103.1 ± 28.7	5
	91	22:09:09.59	-27:47:36.70	7195	190.4	92	4.2 ± 1.9	332.1 ± 49.3	4
3	30	04:36:24.21	-02:50:42.39	4645	105.0	61	1.9 ± 0.5	255.0 ± 21.1	4
	90	22:02:04.47	-31:56:17.88	2635	109.9	33	1.5 ± 0.6	237.9 ± 29.6	4
	97	23:47:23.91	-02:18:43.08	6579	342.2	85	23.5 ± 1.9	591.1 ± 16.2	5

**Notes.** Columns list: (1) the HCG phase; (2) the HCG group ID; (3) the J2000 co-ordinates as computed from this work (see Sect. 3.3); (4) the heliocentric systemic velocity from Jones et al. (2023); (5) the group's velocity dispersion; (6) the group's distance from Jones et al. (2023); (7) the virial mass of the group; (8) the virial radius of the group based on its velocity dispersion; (9) the number of group members considered. See text for details on derived properties.

**Table 2.** Parameters of the HCG HI cubes observed with MeerKAT.

Phase	HCG	$\theta_{\text{maj}} \times \theta_{\text{min}}$	$\theta_{\text{maj}} \times \theta_{\text{min}}$	Noise <sub>3<math>\sigma</math></sub>	N <sub>HI,3<math>\sigma</math></sub>	M <sub>HI,limit</sub>
(1)	(2)	(arcsec <sup>2</sup> )	(kpc <sup>2</sup> )	(mJy beam <sup>-1</sup> )	(10 <sup>18</sup> cm <sup>-2</sup> )	(log M <sub>⊙</sub> )
2	16	57.9 × 57.5	13.8 × 13.3	0.33	3.5	7.3
	31	59.9 × 59.2	15.4 × 14.4	0.33	3.3	7.4
	91	58.0 × 56.1	25.9 × 25.0	0.33	3.7	7.9
3	30	60.5 × 59.8	17.1 × 16.6	0.33	3.3	7.4
	90	57.7 × 56.7	9.3 × 9.0	0.32	3.4	7.0
	97	60.2 × 59.3	23.9 × 23.1	0.32	3.2	7.7

**Notes.** The columns are: (1) the HCG phase; (2) the HCG group ID; (3) the synthesised beam of the considered datacube; (4) the physical scale corresponding to the synthesised beam; (5) the 3 $\sigma$  noise level in the datacube per 5.5 km s<sup>-1</sup> channel; (6) the column density corresponding to the 3 $\sigma$  noise level over a 20 km s<sup>-1</sup> linewidth; (7) the HI mass limit corresponding to the 3 $\sigma$  noise level.

Next, we present a census of the HI in the HCGs in Sect. 4 and evaluate their deficiencies in Sect. 5. Finally, we discuss the observed HI deficiencies as well as their variations in Sect. 6 and summarise the results in Sect. 7. Throughout the paper, we adopt a Hubble constant of  $H_0 = 70 \text{ km s}^{-1} \text{ Mpc}^{-1}$ .

## 2. Sample, HI observations, and data

We have observed six HCGs, with at least four spectroscopically confirmed members, with the MeerKAT telescope. The observations, conducted between July 2021 and January 2022, made use of the telescope's L-band and 32k correlator with a spectral resolution of  $\sim 5.5 \text{ km s}^{-1}$ . Furthermore, to maximise the column density sensitivity, we ensured that at least 61 of the array's 64 antennas were available during the observations.

The target HCG groups were selected to equally represent the main intermediate and late phases (i.e. phase 2 and 3) of the evolutionary sequence (Table 1). Processes responsible for depleting, dispersing, or consuming the gas are most active in phase 2, while phase 3 groups represent the most extreme stages of evolution, raising the most questions about the fate of the HI. We selected three groups in each phase to cover these processes, and to build a cohesive picture of the rapid evolution of HCGs using the new findings we expect to obtain. An extensive description of the observations, as well as of the data reduction, is given in Ianjamasimanana et al. (2025). For each group, several datacubes of varying resolutions were produced to highlight scales of the IGRM. However, for the purpose of this work, we only con-

sider the arcminute-resolution cube<sup>1</sup>, which represents the best compromise between column density sensitivity and resolution.

The HCGs were observed down to a 3 $\sigma$  column density sensitivity of  $\sim 3.2\text{--}3.7 \times 10^{18} \text{ cm}^{-2}$  over 20 km s<sup>-1</sup>, at a restoring beam of about an arcminute (translating to a physical scale of  $\sim 9\text{--}26 \text{ kpc}$ , see Table 2). For each HCG, the HI mass limit corresponding to the 3 $\sigma$  noise level at the centre of the group is given in the table (see Sect. 4.2 for details).

## 3. Optical properties

### 3.1. Optical photometries

Partially because of their location in the southern hemisphere, few galaxies in the vicinity of the selected HCGs are included in existing photometric catalogues. Here, we present new photometric measurements for all galaxies within a 30' radius of the HCGs. Five of the six HCGs fall within the footprint of the DECam Legacy Survey (DECaLS; Dey et al. 2019) DR10<sup>2</sup>. The survey covers the entire South Galactic Cap and the region of the North Galactic Cap at declinations below 34°, reaching an  $r$ -band surface brightness limit of  $\sim 27.9 \text{ mag arcsec}^{-2}$  in the regions of the HCGs. For each of the five HCGs, we have retrieved a  $\sim 1^\circ \times 1^\circ$  cutout image in the  $g$  and  $r$  bands, centred on the group centre. For the last group, HCG 91, only  $g$ - and

<sup>1</sup> Except for HCG 31 where we also use the 15''-resolution datacube for the disc separation, as noted in Sect. 4.1.

<sup>2</sup> <https://www.legacysurvey.org/dr10>



*i*-band images are available; we discuss this at the end of this section.

To perform the photometric measurements from the DECaLS images, we made  $6' \times 6'$  cutouts (enough to cover the spatial extents of the galaxies) centred on each galaxy. We then adapted the procedure described in Wang et al. (2017) and further improved in Lin et al. (2023), which mainly consists of (i) masking the images, (ii) subtracting the background, (iii) constructing a brightness profile and finally (iv) measuring the total flux. In the masking step, we considered the *r*-band images in order to produce mask files with the same pixel sizes as the cutout images. This consisted of masking emissions from all neighbouring sources using the PHOTUTILS package (Bradley et al. 2024). We further deblended interacting sources, mainly in the group cores, to separate the emission of the galaxy of interest from that of the interacting counterparts. The output mask is a combination of two masks, each respectively produced using parameters corresponding to SEXTRACTOR’s ‘cold’ and ‘hot’ modes as described in Rix et al. (2004). While in the ‘cold’ mode, we focus on carefully separating the sources from their neighbours; in the ‘hot’ mode, however, the effort is put into finding and masking stars located away from the galaxy centre.

Next, we performed background subtraction by modelling the image background with a two-dimensional equation. This was then subtracted from the image, and the masked pixels were replaced with the averaged pixel value around the galaxy centre. In the third step, concentric annuli were generated using the geometric parameters obtained from the *r*-band images. The surface brightness was measured as the  $3\sigma$  clipped average value in each of these annuli. However, a condition was set in the outer region of the galaxy to ensure the flattening of the profile: the surface brightness values of 15 contiguous annuli had to be linearly uncorrelated with their sizes. When this condition was met, a  $3\sigma$  clipped average of those 15 values was subtracted as residue background.

Lastly, to estimate the total flux, we simply measured the growth curve of the flux within each annulus as a function of aperture size. Similarly to the surface brightness, the flattening condition had to be met by the flux values of the individual annuli. When this was the case, the total flux of the galaxy was obtained from the  $3\sigma$  clipped average of the fluxes of the outer annuli. This was performed for each of the *g*- and *r*-band images to obtain their respective total fluxes, which were then converted into magnitudes.

For the last group, HCG 91, we retrieved the *r*- and *g*-band magnitudes of galaxies within a  $30'$  radius of the group centre from the photometric catalogues of the fourth Data Release<sup>3</sup> of the Southern Photometric Local Universe Survey (S-PLUS; Mendes de Oliveira et al. 2019). The S-PLUS observations are performed on the robotic telescope T80-South, located at the Cerro Tololo Observatory. The DR4 of S-PLUS includes value-added catalogues, in which star-galaxy-quasar classification and photometric redshifts are provided for millions of objects (Herpich et al. 2024). We proceeded to select all objects falling within the region of HCG 91, detected with a signal-to-noise ratio  $S/N > 3$  and classified as a galaxy with a probability  $\geq 90\%$ . Additionally, to discard background sources, we selected objects with photometric redshift  $\leq 0.03$  (the approximate upper limit for the group’s redshift) and required that the redshift measurement be reliable. The photometric redshift of the S-PLUS detections is estimated through a supervised machine learning algorithm, and the value quoted for a given source in the value-added catalogue

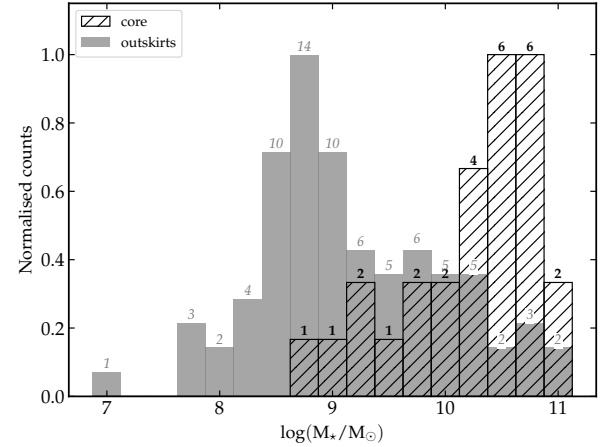


**Fig. 1.** Stellar mass distribution in the HCGs cores (hatched bars) and their surrounding galaxies (solid bars). For visibility, the histograms are normalised by the maximum of each population. The number above each bar represents the absolute count in the corresponding bin.

represents the maximum-a-posteriori estimate from the probability density function (PDF) of the source (Herpich et al. 2024). We define a redshift estimate as reliable if its associated error (the difference between the 16th and 84th percentile values of the PDF) is less than 0.02. For context, this error represents the scatter of the S-PLUS redshift measurements (Lima et al. 2022). Lastly, for a source to be selected, for each candidate galaxy, we check in NED<sup>4</sup> and the DECaLS *g* images for confirmation and search for available properties such as the morphology. A total of 31 galaxies were confirmed in the region of HCG 91 (including the four members of the group), of which we retrieved the *g* and *r* magnitudes from the S-PLUS catalogue.

Finally, we corrected all magnitudes for Galactic extinction based on the dust map of Schlegel et al. (1998).

### 3.2. Stellar masses

To estimate the stellar masses of the galaxies, we took advantage of their intrinsic relation with the galaxy colour. Thus, by considering the *r*-band absolute magnitude  $M_r$  and the *g* – *r* colour of the galaxies, we used the equation:

$$\log(M_{\star}/M_{\odot}) = a_r(g - r) + b_r - 0.4(M_r - M_{r,\odot}), \quad (1)$$

where  $M_{r,\odot} = 4.65$  is the Sun’s absolute magnitude in the *r*-band (Willmer 2018) and  $a_r = 1.49$  and  $b_r = -0.70$  were obtained in García-Benito et al. (2019) for a sample of galaxies including various morphological types and spanning a stellar mass range of  $10^{8.4} - 10^{12} M_{\odot}$ . The distribution of the stellar masses in the vicinity of the HCGs is presented in Fig. 1. The most massive galaxies in the sample are located in the group cores, with the surrounding galaxies having a median stellar mass of 1.2 dex lower.

### 3.3. HCG centres

The centre co-ordinates of the HCGs in the literature are from various sources, employing different techniques and considerations to determine the centres of the groups. For example, the central co-ordinates of HCG 16 on NED were computed

<sup>3</sup> <https://splus.cloud/documentation/DR4>

<sup>4</sup> NASA/IPAC Extragalactic Database, <https://ned.ipac.caltech.edu>

by Barton et al. (1996), whose group definition criteria differ from those of Hickson (1982). For a more consistent analysis, we adopt a homogeneous method for estimating the centre of the HCGs based on the positions and stellar masses of their core members. We include in the core all galaxies previously identified as members of the groups, consistently with Jones et al. (2023) and earlier studies. These members were first selected such that the groups contain at least four members within a 3-magnitude range of the brightest galaxy. Furthermore, to ensure compactness and isolation, a limit of  $26 \text{ mag arcsec}^{-2}$  was imposed on the groups' mean surface brightness and the minimum projected distance to the nearest galaxy was set to be three times the radius of the smallest circle containing all members (Hickson 1982). Further studies based on additional images (Hickson et al. 1989) and dynamical properties of galaxies (Hickson et al. 1992) have refined the original catalogue, while ensuring that member galaxies satisfy the above selection criteria. To date, the properties of these groups have been extensively investigated in several studies, with a few claiming that some HCGs may be embedded within larger, looser groups (e.g. Ribeiro et al. 1998; Tovmassian et al. 2006; Mendel et al. 2011; Zheng & Shen 2021). For example, kinematical analyses led by de Carvalho et al. (1997) and Ribeiro et al. (1998) and based on a spectroscopic survey of regions surrounding 17 HCGs, identified potential additional members of the groups, with several containing up to more than a dozen galaxies. In particular, these studies found that HCG 16, 90, and 97 contain seven, nine, and 14 potential galaxy members, respectively. However, as was noted in de Carvalho et al. (1997), it is worth noting that these studies do not apply the selection criteria originally defined in Hickson (1982). Instead, they merely identified galaxies that could potentially belong to larger structures in which the compact groups are embedded. Therefore, in this study, we choose to discard the additional members listed in Ribeiro et al. (1998) and, with the exception of HCG 16 and 31 (see Sect. 4.3), only consider those originally defined in Hickson et al. (1992).

Furthermore, we have searched for additional members following selection criteria similar to those of Hickson (1982) and Hickson et al. (1992), but based on the  $r$ -band photometry derived in Sect. 3.1 and galaxies' systemic velocities compiled from NED. We have considered a galaxy to be an additional core member if (i) its  $r$ -band magnitude is within a 3-magnitude range of the brightest member, (ii) its projected separation from the group's centre is less than twice the median pairwise galaxy separation, and (iii) its systemic velocity is within three times the group's velocity dispersion. Condition (i) is similar to that imposed in Hickson (1982) and condition (iii) is a more conservative limit of the range of redshift distribution of  $1000 \text{ km s}^{-1}$  calculated in Hickson et al. (1992). Moreover, condition (ii) was further imposed to prevent adding galaxies spatially isolated from the group. We note that these criteria are not intended to mimic those of the original studies; instead, we wish to include in the core any additional galaxy that presents a high probability of being dynamically associated with the group, rather than being a chance alignment. Of the HCGs included in this study, only two galaxies (ESO466-G044 and ESO466-G046; see Fig. 2) in the surroundings of HCG 90 satisfy these criteria. They are respectively classified as lenticular and early spiral, and located at respective systemic velocities of  $\Delta v = 183$  and  $-317 \text{ km s}^{-1}$  away from the group's centre. Both galaxies were previously identified by de Carvalho et al. (1997) as potential members (respectively denoted HCG 90-06 and 90-05 therein) of the group, along with three other galaxies located in the surrounding. However, Ribeiro et al. (1998) further suggested that

HCG 90 and 97 are likely central parts of loose groups extending beyond their boundaries (see also Tovmassian et al. 2006), explaining the abundance of galaxies in the surroundings of these groups. Since no clear evidence of interaction with the rest of the core members of HCG 90 is seen in neither ESO466-G044 or ESO466-G046, we choose to not include them in the core for the rest of the present study. Instead, we classify them as outskirts, together with all other galaxies in the surroundings. We remind the reader that the purpose of this exercise is not to redefine the HCGs, but to gain insights into the distribution HI content in these groups and across their evolutionary path. Therefore, we expect that a limited margin of error in the core/outskirts classification will not significantly impact the results derived from the analysis presented in this work (see Appendix B).

For each group, we define the central co-ordinates as the centre of mass of the group:

$$\mathbf{P} = \frac{\sum_i m_i \mathbf{p}_i}{\sum_i m_i}, \quad (2)$$

where  $\mathbf{p}_i$  and  $m_i$ , respectively, represent the position and stellar mass of member galaxy  $i$ . The updated group centre co-ordinates are listed in Table A.1 and their position relative to the literature values in Fig. 2. The separation between the two positions is negligible for phase 2 groups; however, for phase 3 groups, we note a significant separation ( $>0.8'$ ) of the updated positions with those of the literature.

The size of the groups can be characterised in different ways: by considering the radius of the circle encompassing the centres of the galaxy members (e.g. Hickson 1982; de Carvalho et al. 1997), the median group pairwise separation (e.g. Hickson et al. 1992; Ribeiro et al. 1998) or simply through the virial radius. We opted for the latter as it not only accounts for the projected separations between the individual members, but also for the distributions of their radial velocities. We first estimate the total mass of the group through the approximation of the virial mass of Heisler et al. (1985, Eq. (4))

$$M_{\text{vir}} = \frac{3\pi N}{2G} \frac{\sum_i^N (v_i - V_{\text{sys}})^2}{\sum_{i < j} \frac{1}{r_{ij}}}, \quad (3)$$

where  $N$  is the total number of galaxy members in the group,  $G$  the gravitational constant, and  $v_i$  and  $V_{\text{sys}}$ , respectively, the systemic velocities of galaxy  $i$  and the group and  $r_{ij}$  the pairwise projected separation between members  $i$  and  $j$ . For simplicity, the equation assumes that all group members have equal masses, such that the group's centroid coincides with its gravitational centre. Of course, this is a simplification of the actual picture of the dark matter halo encompassing the galaxies in the groups. However, consequently to the selection criteria imposed on the HCG galaxies, the core members span at most an order of magnitude in stellar mass (see Table A.2; the groups that exhibit the largest variation in member  $\log M_{\star}$  values are HCG 30 and 97, with ranges of 1.1 and 1.0 dex, respectively). Furthermore, as was noted in Heisler et al. (1985), the approximation provides good mass estimates even if the galaxies have a range of masses. To evaluate the uncertainty on the total mass, we perform a simple error propagation on Eq. (3) in which we neglect the errors on the pairwise separations  $r_{ij}$  (the positions of the member galaxies are determined with high accuracies), which gives

$$\delta M_{\text{vir}} = M_{\text{vir}} \frac{\delta X_v}{X_v}, \quad (4a)$$



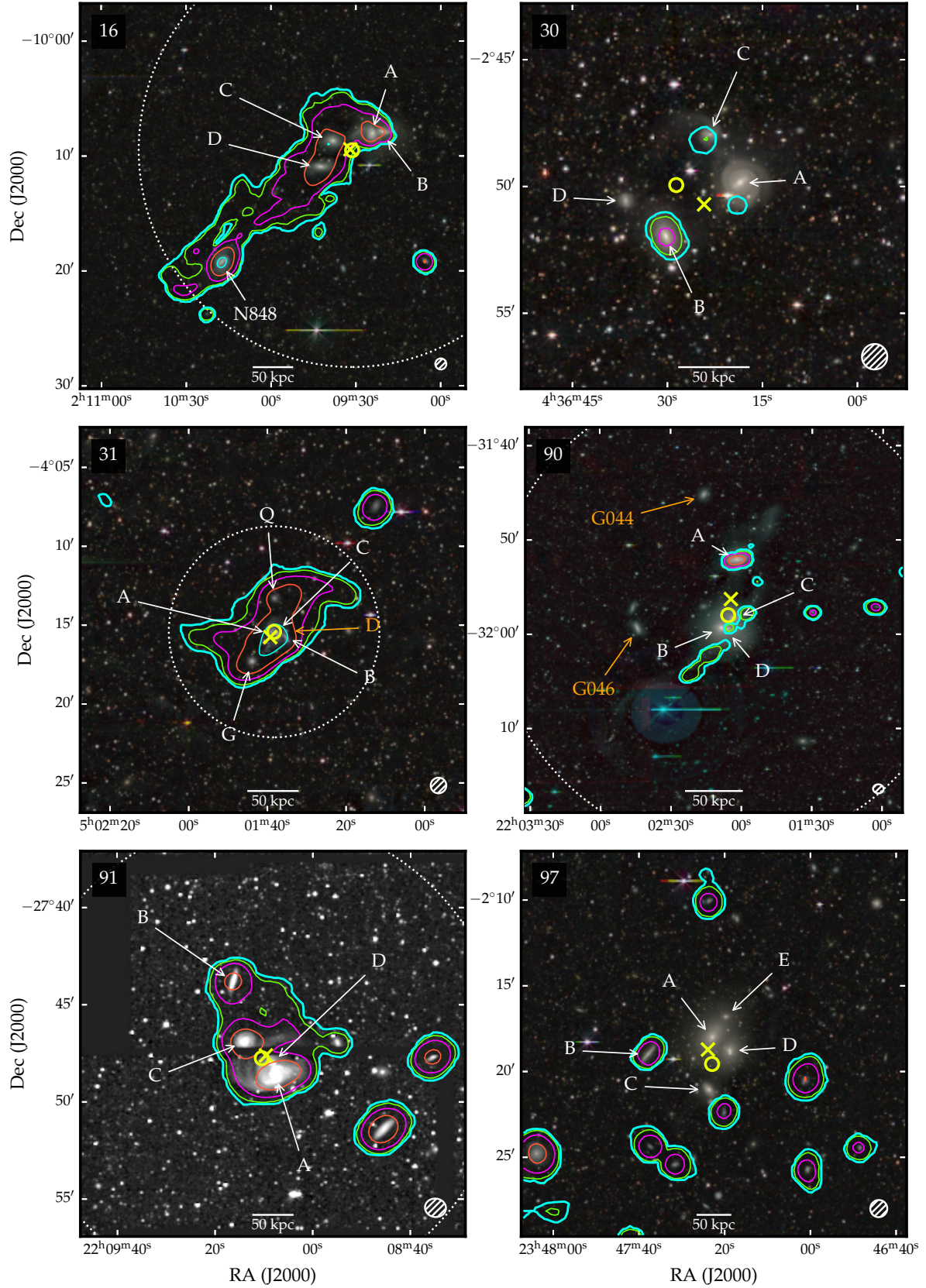


**Fig. 2.** HI contours of the central regions of the phase 2 (left) and 3 (right) HCGs overlaid on their optical *grz* colour images from DECaLS (except for HCG 91 where the only DECaLS *g*-band image is shown). The contours are at  $N_{\text{HI},3\sigma} \times 2^{2n}$ , with  $N_{\text{HI},3\sigma}$  given in Table 2 and  $n = 0, 1, 2, 3$ , respectively, for the cyan, green, magenta, and orange contours. The core galaxies are labelled with white letters, and the yellow circle and cross, respectively, show the NED and calculated positions of the group centres. The objects G044 and G046 in HCG 90's panel correspond respectively to ESO466-G044 and ESO466-G046 (see Sect. 3.3 for details). The dotted circle shows the group's virial radius where it can be seen. The HCG number is given in the upper left corner of each panel and the synthesised HI beam is represented by a hatched ellipse in the lower right corner.

with

$$X_v = \sum_i^N (v_i - V_{\text{sys}})^2, \quad (4b)$$

$$\delta_{X_v} \approx 2 \sqrt{\sum_i (v_i - V_{\text{sys}})^2 \delta_{v_i}^2 + \left[ \sum_i (v_i - V_{\text{sys}}) \right]^2 \delta_{V_{\text{sys}}}^2}. \quad (4c)$$

Here,  $\delta_{v_i}$  and  $\delta_{V_{\text{sys}}}$  are respectively the uncertainties on  $v_i$  and  $V_{\text{sys}}$ . We assume a 2% error on  $v_i$  (more conservative than the typical values reported on NED) and we choose the error on  $V_{\text{sys}}$  to be the standard error of the mean velocity, that is,  $\sigma_v / \sqrt{N}$  ( $\sigma_v$  here denotes the group's velocity dispersion). Next, from the total mass, we follow the virial theorem and estimate the radius as

$$r_{\text{vir}} = \left( \frac{G M_{\text{vir}}}{100 H_0^2} \right)^{1/3} \quad (5a)$$

and its estimated uncertainty as

$$\delta_{r_{\text{vir}}} = \frac{r_{\text{vir}} \delta_{M_{\text{vir}}}}{3 M_{\text{vir}}}. \quad (5b)$$

The values of  $M_{\text{vir}}$  and  $r_{\text{vir}}$ , as well as their respective errors, are given in Table 1. It is important to note that HCGs are likely not fully relaxed and virialised structures (e.g. Da Rocha et al. 2008). As a consequence, our estimate of  $r_{\text{vir}}$  should be interpreted as a measure of the scale of the influence of the HCG environment, rather than a measure of the actual virial radius of the HCG host halo.

## 4. H<sub>I</sub> Census in HCGs

### 4.1. Separating H<sub>I</sub> features

The intermediate phase groups contain large H<sub>I</sub> envelopes encompassing several of their members, making it difficult to trace the extent of their gas disc. To estimate the approximate H<sub>I</sub> content in the discs of the groups' individual galaxy members, we follow the method of Jones et al. (2023) to attempt a feature separation. This involves creating manual 3D masks of the galaxy discs thanks to the visualisation tool SLICERASTRO (Punzo et al. 2017). The H<sub>I</sub> discs of all galaxies in phase 2 groups were successfully separated from the envelope, except for HCG 91D which was not detected. As for HCG 31, the limited angular size of the group made it impossible to distinguish the discs of its members in the 60''-resolution datacube. Thus, we performed the separation on the highest-resolution (15'') cube, enabling the extraction of five core members from the envelope (HCG 31A, B, C, G and Q).

### 4.2. H<sub>I</sub> masses

The H<sub>I</sub> mass was calculated from the total line flux density,  $S \Delta v$ , and luminosity distance,  $D$ , as

$$\frac{M_{\text{H}_I}}{M_{\odot}} = 2.36 \times 10^5 \left( \frac{D}{\text{Mpc}} \right)^2 \frac{S \Delta v}{\text{Jy km s}^{-1}}. \quad (6)$$

The line flux was measured from the total intensity map (zeroth moment) produced by SoFIA<sup>5</sup> (H<sub>I</sub> Source Finding

Application; Serra et al. 2015; Westmeier et al. 2021) and the distance taken from Jones et al. (2023). The line flux measurement for individual galaxies was straightforward, as the extent of their H<sub>I</sub> disc is unambiguous. However, for galaxies whose H<sub>I</sub> discs were connected in H<sub>I</sub>, the manually constructed three-dimensional masks discussed in Sect. 4.1 were used to identify emission belonging to the discs.

There are, however, several galaxies that were not detected in the MeerKAT H<sub>I</sub> data. For these, two possibilities arise: either they are devoid of atomic gas, or their H<sub>I</sub> content is not sufficiently high to be detected in the MeerKAT observations. Assuming the second hypothesis, we determined the maximum H<sub>I</sub> content possible for these galaxies. This content, referred to as the detection limit, was evaluated as follows: first, we built a noise map of the observed region by computing the median of the noise cube produced by SOFIA at each spatial position. Then, we calculated the noise level at the spatial position of the galaxy by considering an area of the noise map the size of a beam and a velocity width equivalent to 20 km s<sup>-1</sup>. Finally, we derived the H<sub>I</sub> mass corresponding to the 3 $\sigma$  noise using Eq. (6).

Fig. 3 shows the H<sub>I</sub>-stellar mass relation for galaxies in the vicinity of all six groups, compared to a sample of 518 isolated galaxies (Bok et al. 2020). These galaxies were selected from the Analysis of the interstellar Medium in Isolated GALaxies (AMIGA; Verdes-Montenegro et al. 2005a) project, a well-defined sample of strictly isolated galaxies drawn from the Catalogue of Isolated Galaxies (CIG; Karachentseva 1973). The isolation criteria imposed on AMIGA galaxies are more conservative than those considered in the original CIG sample, based on two isolation parameters,  $\eta$  and  $Q$ , evaluating the surface density of neighbours out to the fifth nearest neighbour and the tidal force exerted by neighbouring galaxies, respectively. Multi-wavelength studies of the AMIGA galaxies, conducted over the past two decades, have demonstrated that the sample exhibits the lowest levels of all properties that are enhanced by interactions (e.g. Lisenfeld et al. 2007, 2011; Leon et al. 2008; Espada et al. 2011; Jones et al. 2018; Sorgho et al. 2024). This property establishes AMIGA as the most reliable baseline in the literature for evaluating the normalcy of H<sub>I</sub> content of galaxies and assessing the influence of environmental interactions on this content.

For each of the groups, the total mass of the H<sub>I</sub> emission contained in the core of the group was also measured (coloured squares in Fig. 3). This includes both the H<sub>I</sub> from the galaxies making up the core and that in the IGrM. Because most phase 3 group members (filled warm-coloured circles) are undetected in H<sub>I</sub>, their estimated total core H<sub>I</sub> masses are more than an order of magnitude lower than those of phase 2 groups (filled cool-coloured circles). However, no systematic difference is observed in the H<sub>I</sub> masses of the outskirts galaxies of both phases (coloured crosses).

### 4.3. Phase 2 or intermediate-phase groups

Earlier studies showed that intermediate phase groups still possess a significant amount of gas in their cores (Verdes-Montenegro et al. 2001; Jones et al. 2023). The left panel of Fig. 2 shows the H<sub>I</sub> distribution in the core of the three observed HCGs, and the H<sub>I</sub> masses of their members are summarised in Table 3. Below, we give a brief description of the individual groups and their surrounding galaxies. We note that the search for surrounding galaxies was limited within a maximum separation of 1000 km s<sup>-1</sup> from the HCG systemic

<sup>5</sup> Version 2, <https://gitlab.com/SoFIA-Admin/SoFIA-2>



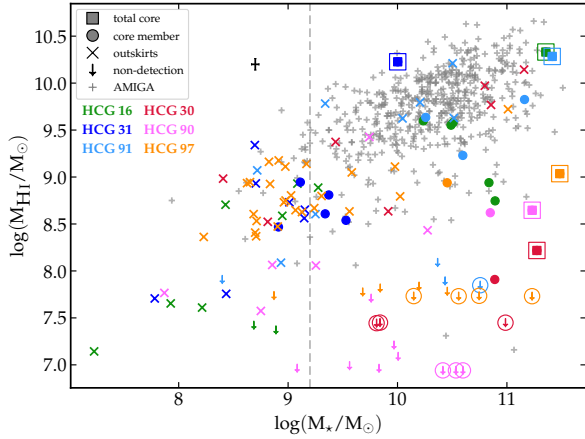


**Fig. 3.** HI-stellar mass relation of the galaxies in the compact group regions (colour symbols) and of the isolated galaxies of the AMIGA sample (grey crosses). The vertical dashed line at 9.2 dex shows the lower mass limit of the AMIGA galaxies.

velocities to avoid including foreground and background galaxies.

#### 4.3.1. HCG 16

The core of HCG 16 is formed by five galaxies (HCG 16A, 16B, 16C, 16D and NGC 848) embedded in an envelope spanning  $\sim 24'$  across, or a projected distance of  $\sim 342$  kpc, with a total HI mass of  $2.1 \times 10^{10} M_{\odot}$ . The fifth member, NGC 848, was not initially included in Hickson (1982)'s catalogue, but was identified by de Carvalho et al. (1997) and was later observed to be connected to the four other members in HI (Verdes-Montenegro et al. 2001). In projection, the early spirals (Sa) 16A and 16B form the closest pair, although they are  $>200 \text{ km s}^{-1}$  away from one another. Despite its high infrared luminosity and close projected proximity to 16B, early H $\alpha$  studies found that 16A presents no signs of recent interactions in its inner disc (e.g. Mendes de Oliveira et al. 1998). At an angular distance of  $\sim 3'$  east of the pair, lies the third member 16C – itself located  $\sim 2'$  northwest of 16D. The most distant member of the core, NGC 848, is a barred early spiral of a similar size that lies  $\geq 10'$  southeast of 16D. All galaxies making up the system are thought to either be starburst-dominated or have active galactic nuclei (AGNs; Ribeiro et al. 1996; Turner et al. 2000), with the pair 16A and 16B confirmed to be hosting AGNs (O'Sullivan et al. 2014; Oda et al. 2018). Outside this collection of galaxies and within a radius of  $30'$  ( $\sim 428$  kpc), seven HI-bearing galaxies were detected with HI masses ranging from  $1.4 \times 10^7 M_{\odot}$  to  $8.5 \times 10^8 M_{\odot}$ . All these detections are within  $147 \text{ km s}^{-1}$  of the group's systemic centre, except for the object 'PGC 4584000' located  $814 \text{ km s}^{-1}$  away ( $\sim 8$  times the velocity dispersion) in the foreground.

#### 4.3.2. HCG 31

Unlike in HCG 16, the objects forming the HCG 31 group are actively star-forming galaxies exhibiting signs of recent or ongoing interactions (e.g. Iglesias-Paramo & Vilchez 1997; Amram et al. 2007; Alfaro-Cuello et al. 2015). The group has a core mass of  $1.7 \times 10^{10} M_{\odot}$  spread over five galaxies (HCG 31A, B, C, G and Q) and several tidal features. Initially, HCG 31 was thought to host four members (31A, B, C and D; Hickson 1982); however, as our understanding of its structure improved thanks to

**Table 3.** HI masses of individual HCG core members.

HCG	Member	$\log M_{\text{HI,gal}}$ ( $M_{\odot}$ )	$\log M_{\text{HI,ext}}$ ( $M_{\odot}$ )
16	16A	8.7	–
	16B	8.9	–
	16C	9.6	–
	16D	9.6	–
	N0848	9.6	–
	<b>Total</b>	<b>10.1</b>	<b>9.9</b>
31	31A	8.5	–
	31B	8.9	–
	31C	8.8	–
	31G	8.6	–
	31Q	8.5	–
	<b>Total</b>	<b>9.4</b>	<b>10.2</b>
91	91A	9.8	–
	91B	9.2	–
	91C	9.6	–
	LEDA 749936 <sup>(*)</sup>	8.2	–
	<b>Total</b>	<b>10.1</b>	<b>9.8</b>
30	30A	$<7.4$	–
	30B	7.9	–
	30C	$<7.5$	–
	30D	$<7.4$	–
	<b>Total</b>	<b><math>\leq 8.2</math></b>	–
90	90A	8.6	–
	90B	$<6.9$	–
	90C	$<6.9$	–
	90D	$<6.9$	–
	<b>Total</b>	<b><math>\leq 8.6</math></b>	<b>8.2</b>
97	97A	$<7.7$	–
	97B	8.9	–
	97C	$<7.7$	–
	97D	$<7.7$	–
	97E	$<7.7$	–
	<b>Total</b>	<b><math>\leq 9.0</math></b>	–

**Notes.** The top and bottom halves respectively include the phase 2 and 3 groups. The last two columns respectively list the HI masses inside and outside the discs of the member galaxies. <sup>(\*)</sup>LEDA 749936 (WISEA J220854.95-274701.6) coincides spatially with the peak of an HI cloud in the core of HCG 91, but lacks an optical readshift; we include it in this table but do not count it as a core member.

the availability of multi-wavelength data, the group was reconfigured to include new members (Rubin et al. 1990) and reject 31D (which happens to be a background galaxy<sup>6</sup>; Hickson et al. 1992). Morphologically, the members of HCG 31 comprise three late spirals (A, B and C) and two irregulars (G and Q) spanning the velocity range  $3990\text{--}4136 \text{ km s}^{-1}$ . Apart from these main galaxies, there is a complex of three emission line, star-forming regions E, F and H (Rubin et al. 1990; Gallagher et al. 2010; Gómez-Espinoza et al. 2023) in the southern region of the group, associated with a prominent HI tail (Verdes-Montenegro et al. 2005b). The current MeerKAT observations reveal that the HI structure encompassing the members of the group spans an angular size of  $\sim 8.9'$ , translating to a projected distance of  $\sim 137$  kpc at the group's distance. In a  $30'$ -radius ( $\sim 462$  kpc) of the group's centre five galaxies were detected in HI; we also detected two additional galaxies beyond this radius and within a maximum separation of  $\sim 825$  kpc. The HI masses of all seven

<sup>6</sup> The approximate position of HCG 31D is given in Fig. 2.

surrounding galaxies range from  $5.1 \times 10^7 M_{\odot}$  to  $2.2 \times 10^9 M_{\odot}$ , with a maximum radial separation of  $438 \text{ km s}^{-1}$ .

#### 4.3.3. HCG 91

HCG 91 is a quartet of late-type galaxies (91A–D), dominated by the barred face-on spiral, 91A, interacting with a fainter companion, 91D. Moreover, optical images of 91A show the presence of a prominent tidal tail in the galaxy pointing towards 91C (Eigenthaler et al. 2015). Early studies of the group have revealed that both these members host H $\alpha$ -emitting regions, presenting highly disturbed velocity fields in their inner discs (González Delgado et al. 1997; Amram et al. 2003). Further spectroscopic studies of 91C have detected rapid variations in the oxygen abundance in the arms of the galaxy, providing evidence for gas infall and interstellar medium (ISM) enrichment along the arms of 91C (Vogt et al. 2015, 2017). The core of the group is similar to those of the other two intermediate phase groups in terms of HI content: it has a mass of  $1.9 \times 10^{10} M_{\odot}$  distributed over an envelope of length  $\sim 10'$  (267 kpc). The envelope extends to a cloud located west of the group, whose peak coincides with the optical object LEDA 749936. However, since no redshift information is available for the optical counterpart, we do not include it in the core. One of the four members, 91D, overlapping in projection with 91A, is not detected in HI (Jones et al. 2023). Outside the core, we have detected six galaxies within a  $30'$  radius ( $\sim 803 \text{ kpc}$ ) and an additional five within  $\sim 1141 \text{ kpc}$ . The maximum largest velocity separation with the group's centre is  $381 \text{ km s}^{-1}$ . The HI masses of the detections range from  $1.2 \times 10^8 M_{\odot}$  to  $8.5 \times 10^9 M_{\odot}$ .

#### 4.4. Phase 3 or late-phase groups

Unlike the intermediate phase, groups in the late stage of the evolutionary sequence tend to exhibit a high HI deficiency, most likely as a result of their advanced evolution stage. In the right panel of Fig. 2 we show an overview of the HI morphology in the groups and in Table 3 we list the estimated HI mass of their members.

##### 4.4.1. HCG 30

The core of HCG 30 consists of four galaxies in a quadrilateral shape with a  $\sim 6'$  (about 106 kpc) diagonal: HCG 30A, 30B, 30C and 30D. Except 30C, which is identified as an intermediate-late spiral (Sbc), all galaxies of the quartet are early spirals. Previous interferometric HI studies have found that HCG 30 is among the most HI-deficient groups (Verdes-Montenegro et al. 2001; Jones et al. 2023), although no clear evidence for diffuse hot gas was found in its IGrM (Rasmussen et al. 2008; Desjardins et al. 2014). Unlike past observations where no member of the group was detected in HI, we unambiguously uncover HI in 30B, with a mass of  $8.1 \times 10^7 M_{\odot}$ . Moreover, HI emission is detected for the first time at the respective spectral positions of 30A and 30C, but with a spatial offset peak with respect to their centres.

A total of seven HI-bearing galaxies are located around the core of the group, five of which fall inside the  $30'$ -radius (532 kpc) and the other two within a 866 kpc separation. Their HI masses range from  $3.3 \times 10^8 M_{\odot}$  to  $1.4 \times 10^{10} M_{\odot}$ , with a maximum velocity separation of  $243 \text{ km s}^{-1}$ .

##### 4.4.2. HCG 90

HCG 90 is also a quartet of an early spiral (HCG 90A), two ellipticals (90B and 90C) and an irregular (90D). The most 'isolated'

and northern member of the group, 90A, is a Seyfert galaxy hosting a sub-kpc cold molecular gas ring presenting characteristics of gas outflow (Alonso Herrero et al. 2023). A multi-wavelength study of HCG 90 in the NUV and optical wavelengths enabled the discovery of five low surface brightness (LSB) dwarf galaxy candidates near 90A and 90C (Ordenes-Briceño et al. 2016). Chandra X-ray observations of HCG 90 found diffuse hot gas confined to individual members of the group and forming a bridge between 90B, C and D (Jeltema et al. 2008; Desjardins et al. 2013). Similarly to HCG 30, this group does not show X-ray emission that permeate the IGrM. Consistently with Jones et al. (2023), our MeerKAT observations detect HI in one (90A) of the four members of the group: its measured HI mass is  $4.2 \times 10^8 M_{\odot}$ . Furthermore, an HI stream of mass  $2.1 \times 10^8 M_{\odot}$ , seemingly aligned with an optical structure, is detected across the central members of the group. This feature is discussed in Ianjamasimanana et al. (2025). Among the surrounding galaxies of the group, three were detected in HI inside a  $30'$  radius (288 kpc) and an additional three within  $\sim 402 \text{ kpc}$  (all located within  $435 \text{ km s}^{-1}$  of the group centre).

##### 4.4.3. HCG 97

Two ellipticals (HCG 97A and 97D), a late spiral (97B), and two early spiral (97C and 97E) galaxies constitute the core of HCG 97, all lying within the velocity range  $6003\text{--}6932 \text{ km s}^{-1}$ . Of the six groups studied here, HCG 97 is the least isolated: it has dozens of neighbours within its virial radius and has the largest velocity dispersion ( $\sim 342 \text{ km s}^{-1}$ ). The group is detected in both UV and infrared (Lenić et al. 2016), and X-ray observations show that it has a significantly extended X-ray halo, exhibiting a morphology indicative of recent or ongoing galaxy-galaxy interactions (Mulchaey et al. 2003; Rasmussen et al. 2008; Desjardins et al. 2014). Similarly to the previous phase 3 groups, we find that all galaxies but one are devoid of HI in the group core. The neutral gas-bearing galaxy 97B, has a measured HI mass of  $8.7 \times 10^8 M_{\odot}$ . Recently, Hu et al. (2024) conducted a multi-wavelength study in radio continuum, X-ray and CO(2–1) to demonstrate that 97B is the subject of a ram-pressure stripping scenario, forming a radio emission tail pointing towards the centre of the group. Outside the group core, we have detected 25 galaxies in the MeerKAT observations within  $\sim 742 \text{ kpc}$  ( $30'$ ) and  $855 \text{ km s}^{-1}$  from the centre. An additional galaxy was detected at a projected separation of  $\sim 1058 \text{ km s}^{-1}$ .

## 5. HI deficiency of galaxies in HCGs

### 5.1. Estimating the HI deficiency

HI deficiency, as a measure of the deviation of a galaxy's HI mass from its counterparts, is an important parameter for quantifying the environmental effects on the galaxies' gas content. It is defined as the difference between the galaxy's predicted and actual (or measured) HI masses:

$$\text{def}_{\text{HI}} = \log(M_{\text{HI}}^{\text{pred}}) - \log(M_{\text{HI}}^{\text{obs}}). \quad (7)$$

In this definition,  $\text{def}_{\text{HI}} > 0$  denotes an HI-deficient galaxy while a gas-rich galaxy possesses a negative  $\text{def}_{\text{HI}}$  value.

To estimate the predicted HI mass, we used the almost 'nurture-free' AMIGA sample of isolated galaxies. Thanks to their strict isolation criteria, this sample represents the best baseline for HI normalcy in the absence of interactions. An

$M_{\text{HI}}-L_B$  scaling relation was derived for the AMIGA sample in Jones et al. (2018), enabling the estimate of the expected HI mass of a galaxy within 0.25 dex. However, since we have access to the  $g$ - and  $r$ -band magnitudes of the HCG galaxies rather than their  $B$ -band magnitudes, we re-derived the scaling relation for the  $r$ -band:

$$\log(M_{\text{HI}}^{\text{pred}}/M_{\odot}) = \alpha^T [\log(L_r/L_{\odot}) - 10] + \beta^T, \quad (8)$$

where  $L_r$  is the  $r$ -band luminosity of the galaxy and  $\alpha^T$  and  $\beta^T$  are constants dependent of the RC3 (de Vaucouleurs et al. 1991) morphological type,  $T$ . Similarly to Jones et al. (2018), we define three main morphological classes:  $T < 3$ ,  $3 \leq T \leq 5$  and  $T > 5$ . Of the 844 galaxies included in the Jones et al. (2018) study, 738 have DECaLS photometric measurements in the SGA (Siena Galaxy Atlas; Moustakas et al. 2023) catalogue. These were retrieved through a cross-match between the Jones et al. (2018) sample and the SGA catalogue based on the spatial coordinates. We selected the  $r$  magnitudes of the galaxies at the 26th isophote, which were converted into luminosity via

$$\log(L_r/L_{\odot}) = 10 + 2 \log(D/\text{Mpc}) + 0.4(M_{r,\odot} - r). \quad (9)$$

The HI masses measured in Jones et al. (2018) are from single-dish observations, presumably more sensitive to extended features than interferometric measurements. Of the 738 retrieved galaxies, the HI masses of 205 could not be properly measured; for these, only upper limits were given (see details in Jones et al. 2018). To be consistent with the analysis conducted therein and derive an equivalent HI scaling relation for the  $r$ -band, we similarly account for the upper limits in the linear regression. However, we adopted a Bayesian approach here (instead of the maximum likelihood estimate approach used in Jones et al. 2018) consisting of incorporating both the detections and non-detections, separately, into a likelihood function. We used the Python implementation of the Markov chain Monte Carlo PYMC (version 5.16.2; Abril-Pla et al. 2023), in which we define the Eq. (8) as a linear regression model. The distribution of the detections was modelled as a Normal distribution, whereas for the non-detections we used a Censored distribution defined as

$$f_{Y_c}(y) = \begin{cases} \mathcal{N}(\mu, \sigma) & y < M_{\text{HI},\text{lim}}, \\ 1 - F_Y(\mu_c, M_{\text{HI},\text{lim}}) & y = M_{\text{HI},\text{lim}}. \end{cases} \quad (10)$$

Here,  $\mu = \alpha^T(x - 10) + \beta^T$  models, following Eq. (8), the mean distribution of the predicted HI mass for a given  $x$  and  $\sigma^T$  its associated intrinsic scatter. Furthermore,  $F_Y(\mu_c, M_{\text{HI},\text{lim}})$  represents the probability that a normally distributed variable with ‘censored’ mean  $\mu_c$  is below the HI mass limit  $M_{\text{HI},\text{lim}}$  in the Jones et al. (2018) data. The formulated distribution thus captures the likelihood of observing uncensored values below the HI mass limit and the cumulative probability of the above values.

For each of the free parameters,  $\alpha^T$  and  $\beta^T$ , we chose a Normal distribution of mean  $\mu_N = 0$  and standard deviation  $\sigma_N = 10$  as prior. The large standard deviation was chosen to probe a wide parameter space and ensure that the model is over-constrained. Additionally, the intrinsic scatter,  $\sigma^T$ , was modelled by an Exponential distribution of coefficient 1. In short, the prior distributions are

$$\alpha^T \sim \mathcal{N}(0, 10); \quad \beta^T \sim \mathcal{N}(0, 10); \quad \sigma^T \sim \text{Exp}(1). \quad (11)$$

Finally, 4000 Markov chains were randomly drawn to determine the posterior, from which the best-fit values of the regression

**Table 4.** Linear regression fit results of Eq. (8).

Type	Det.	Non-det.	$\alpha^T$	$\beta^T$	$\sigma^T$
<3	47	99	$1.00 \pm 0.12$	$9.20 \pm 0.06$	$0.57 \pm 0.03$
3–5	363	104	$0.83 \pm 0.06$	$9.42 \pm 0.02$	$0.38 \pm 0.01$
>5	123	2	$0.81 \pm 0.06$	$9.52 \pm 0.04$	$0.30 \pm 0.02$
all	533	205	$0.77 \pm 0.04$	$9.41 \pm 0.02$	$0.42 \pm 0.01$

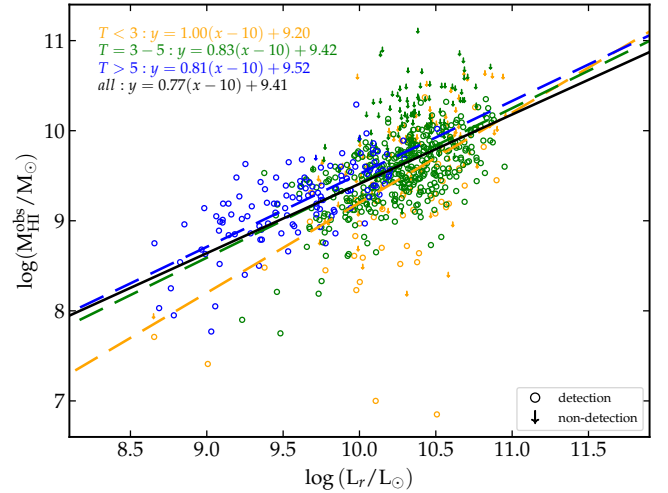


**Fig. 4.** Predicted HI mass as a function of  $r$ -band luminosity of the AMIGA galaxies. The open symbols represent the measured HI masses while the downward arrows denote galaxies for which upper limit masses were considered. The sample is divided into morphology bins, whose fits are shown in dashed lines of corresponding colours. The fit of the overall sample is given by the solid black line.

parameters were derived. This was done for each of the three morphology bins, and the resulting parameters are summarised in Table 4. We present the scatter plot of the  $M_{\text{HI}}-L_r$  of the AMIGA galaxies in Fig. 4, and the posterior distribution for each of the morphological bins in Fig. C.1.

Using Eq. (8) and the parameters in Table 4, we estimated the expected HI masses of the galaxies in the HCGs based on their morphology. These morphologies were taken from the HyperLEDA<sup>7</sup> (Makarov et al. 2014) and NED databases. For galaxies that lack a morphological type in the literature, we performed a visual classification based on their DECaLS colour images. Fig. 5 shows the distribution of the morphologies in the vicinity of the compact groups, for galaxies with optical counterparts.

A striking limitation of the AMIGA sample is that it mainly includes high-mass galaxies, such that very few galaxies of  $M_{\text{star}} \lesssim 10^{9.2} M_{\odot}$  are found in the sample. This is because a systemic velocity cut of  $v_{\text{sys}} > 1500 \text{ km s}^{-1}$  was imposed in the construction of the sample, biasing it against low-mass galaxies. Unfortunately, this bias translates into an under-prediction of the gas content of low-mass galaxies in the HCG galaxies. This is a direct consequence, as has been demonstrated in several studies (e.g. Maddox et al. 2015; Hunt et al. 2020), of the break in the HI-to-stellar mass relation at stellar mass orders of  $\sim 10^9 M_{\odot}$ , where galaxies transition between gas-dominated and stellar-dominated baryonic discs. Galaxies below this mass range exhibit higher HI-to-stellar mass fractions than more massive galaxies. To account for these systematic differences

<sup>7</sup> <http://atlas.obs-hp.fr/hyperleda>



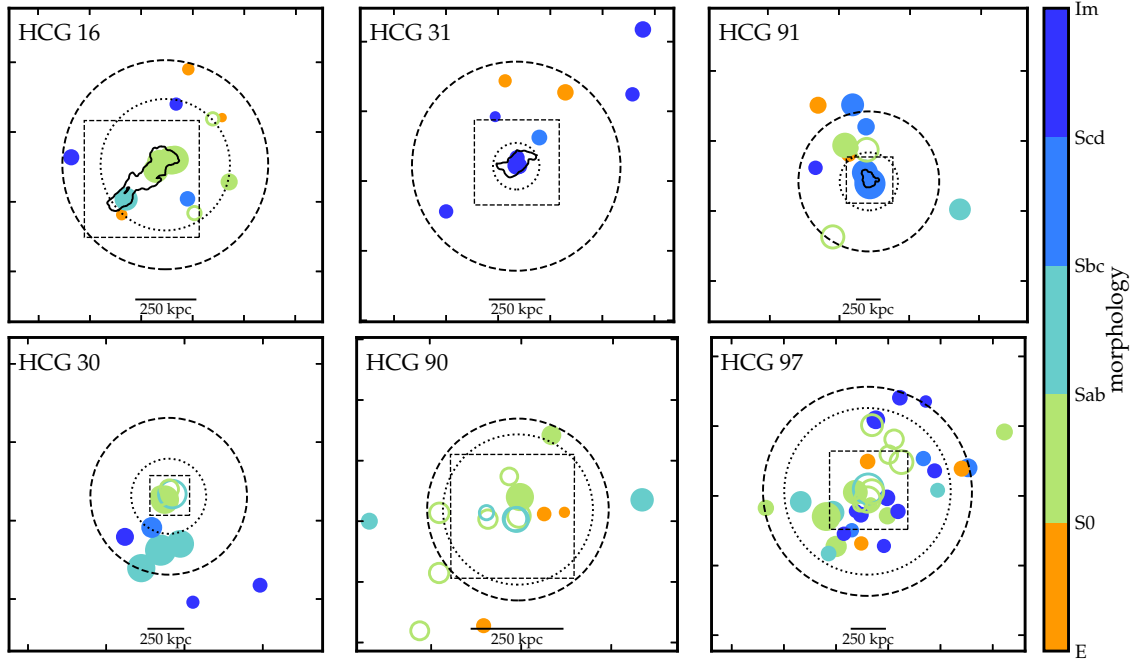


**Fig. 5.** Morphology distribution in and around the HCGs. In the phase 2 groups (top panels) are shown the outermost contours of Fig. 2. The dashed box corresponds to the area covered in Fig. 2 and the dotted and dashed circles show respectively the virial radius  $r_{\text{vir}}$  and the  $30'$  FWHM of MeerKAT. The size of the symbols is proportional to the stellar mass. Filled symbols represent sources detected in HI, while open circles are non-detections.

between low- and high-stellar mass galaxies, we employed a separate method to estimate the predicted HI mass of our sample galaxies below  $10^{9.2} M_{\odot}$ . For this, we made use of the HI-to-stellar mass relation of Bradford et al. (2015):

$$\log(M_{\text{HI}}^{\text{pred}}/M_{\odot}) = \begin{cases} 1.05 \log(M_{\star}/M_{\odot}) + 0.09 & M_{\star} < 10^{8.6} M_{\odot}, \\ 0.46 \log(M_{\star}/M_{\odot}) + 5.18 & \text{otherwise.} \end{cases} \quad (12)$$

The relation was derived from a sample of isolated galaxies selected from the NASA Sloan Atlas (Blanton et al. 2011) catalogue, focusing on 368 low-mass galaxies spanning the stellar mass range  $10^7$ – $10^{9.5} M_{\odot}$ . We note that Bradford et al. (2015) use a different definition of isolation than AMIGA, solely based on its separation from its closest neighbour. Specifically, they define a low-mass galaxy ( $M_{\star} < 10^{9.5} M_{\odot}$ ) as isolated if it is located more than 1.5 Mpc from a massive host. Their analysis revealed a break in the HI-to-stellar mass relation at stellar masses of  $10^{8.6} M_{\odot}$  (just below the range found in Maddox et al. 2015), which the authors attribute to differences in internal processes (such as star formation efficiencies and gas temperatures) of low- and high-mass galaxies. In total, 45 of the 135 galaxies in our HCG sample have stellar masses  $< 10^{9.2} M_{\odot}$ , whose predicted  $M_{\text{HI}}$  were hence estimated by Eq. (12). These galaxies are essentially surrounding objects, with the exception of a core galaxy (HCG 31Q). The HI deficiencies of the individual HCG galaxies, as well as their optical properties, are given in Table A.2. Likewise, those of the surrounding galaxies (including non-detections) are listed in Table A.3. To summarise, three stellar mass bins were considered in the evaluation of the predicted HI mass:

- for  $M_{\star} < 10^{8.6} M_{\odot}$ , we use the first line of Eq. (12);
- for  $10^{8.6} M_{\odot} < M_{\star} < 10^{9.2} M_{\odot}$ , we use the second line of Eq. (12);

- for  $M_{\star} > 10^{9.2} M_{\odot}$ , we use Eq. (8) with parameters in Table 4.

Similarly to Verdes-Montenegro et al. (2001) and Borthakur et al. (2010), we approximate the predicted mass of a galaxy group as the sum of the predicted individual masses. This is especially important for the intermediate phase groups (HCG 16, 31 and 91) whose central members are embedded in large HI envelopes. Their core HI deficiency was thus obtained by comparing the HI mass contained in the core envelopes to the total predicted mass of the core members.

Fig. 6 shows the comparison of the measured and predicted HI masses of all galaxies in a  $\sim 30'$  radius around the HCGs. Two facts are important to highlight in the figure: first, the total HI contained in the cores of the late-phase groups are below the predicted values. This is in line with the expectations since most galaxies in these cores lack atomic gas (this is further shown by the individual galaxies in these cores having measured HI masses below their predicted masses). On the other hand, the total measured HI masses in the cores of intermediate-phase groups are within the predicted values, signifying that these cores are HI-normal. Secondly, the outskirts galaxies around phase 2 groups are not segregated from those around phase 3 groups in this parameter space. We further discuss this in Sect. 6.2.

## 5.2. Distribution of HI deficiency in HCGs

In their study of 38 HCGs with available HI observations, Jones et al. (2023) proposed a revised evolutionary sequence of the HCGs, expanding the earlier work of Verdes-Montenegro et al. (2001) with an additional sub-phase in the last stage of the compact group evolution. In the additional sub-phase, a single galaxy is found to bear HI in an otherwise HI-devoid group, and where the extended features (if any) represent less than 25% of all the detected HI. More importantly, the authors find that while the HI deficiency is similar in the

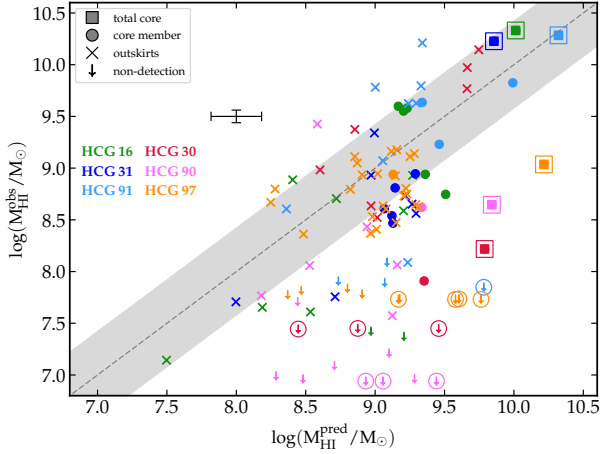


**Fig. 6.** Predicted vs measured HI masses of galaxies in the HCGs. The dashed line and shaded region represent the one-to-one relation and intrinsic scatter of Eq. (8), respectively.

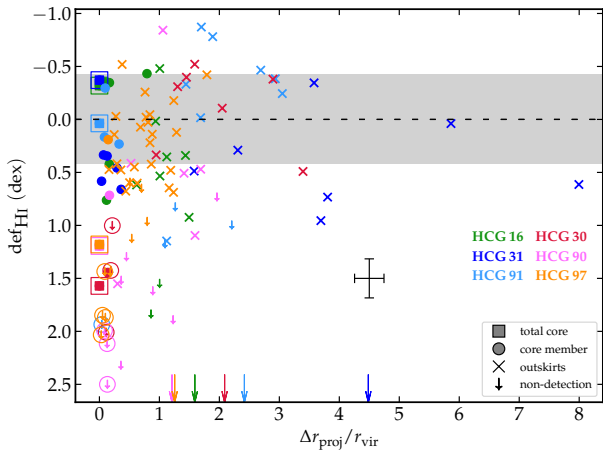


**Fig. 7.** HI deficiency vs projected distance from group centre in units of  $r_{\text{vir}}$  for galaxies in and surrounding HCGs. The shaded region, corresponding to the scatter in Fig. 6, represents the zone of ‘normal’ HI content.

early and intermediate phases of HCGs (phases 1 and 2), the late-phase groups exhibit deficiencies about 1.5 dex higher than the previous two. However, a clear picture of the HI-deficiency – or, conversely, the HI-richness – of the HCGs with respect to their surroundings remains to be uncovered.

Taking advantage of MeerKAT’s short baselines and large field of view, we aim to obtain a uniform view of the atomic gas content of the HCGs and their immediate vicinity, probing the HI in galaxies out to at least one virial radius,  $r_{\text{vir}}$ . In Fig. 7 we show the variation in the HI deficiency with the projected distance (normalised by  $r_{\text{vir}}$ ) from the group centre. The first fact worth noting in the figure is the segregation between phase 2 (cool-coloured circles) and phase 3 core galaxies (warm-coloured circles), with the former possessing normal HI content and the latter being highly deficient. This is a direct consequence of the trend observed in Fig. 6, and in line with the HI-to-stellar mass variations of Fig. 3. Secondly, in both phases, we observe a moderate reduction in HI deficiency (indicating an increase in the atomic gas fraction) with increasing radial distance, out to one virial radius. To assess the existence of a correlation between the  $\text{def}_{\text{HI}}$  and the radius, we performed a Spearman’s Rank test by calculating the correlation coefficient,  $\rho_{\text{def}_{\text{HI}}, r_{\text{proj}}}$ , of the galax-

ies in the outskirts; that is, the galaxies not considered to be HCG members. We obtained a coefficient of  $-0.28$  with a statistical  $p$ -value  $= 1.2 \times 10^{-2}$ , indicative of a weak correlation between the two variables. We further split the sample into galaxies within the virial radius and those outside, and found median  $\text{def}_{\text{HI}}$  values of  $0.47 \pm 0.11$  dex and  $0.12 \pm 0.11$  dex respectively for  $r < r_{\text{vir}}$  and  $r > r_{\text{vir}}$ . We repeated the exercise for the phase 2 and 3 groups separately, finding similar results, although with higher  $p$ -values (0.1 and 0.05, respectively for phase 2 and 3) suggest a lower probability for monotonic trends. Nonetheless, a similar trend of  $\text{def}_{\text{HI}}$  values inside and outside the virial radius is observed for both phases individually.

## 6. Discussion

Quantifying the HI-normalcy of a galaxy depends on the adopted definition, which may vary according to methodological preferences. For example, while several studies define HI-normal galaxies as those having  $\text{def}_{\text{HI}}$  values within a multiple of the scatter in the HI mass scaling relation (e.g.  $2\sigma$  in Solanes et al. 2002 and Denes et al. 2014,  $1\sigma$  in Jones et al. 2023), others adopt a characteristic threshold value for  $\text{def}_{\text{HI}}$  (e.g. Solanes et al. 2001 use  $\text{def}_{\text{HI}} > 0.3$  to quantify HI-deficient galaxies, corresponding to two times the predicted HI content).

In this study, we define a galaxy as normal if its deficiency parameter is within  $\pm 0.42$  dex (corresponding to the scatter of Eq. (8) for all galaxies, see Table 4), that is, its measured mass is within the interval  $0.4 M_{\text{HI}}^{\text{pred}} < M_{\text{HI}}^{\text{obs}} < 2.6 M_{\text{HI}}^{\text{pred}}$ ; similarly, it is deficient (rich) if  $\text{def}_{\text{HI}}$  is above (below) these limits.

### 6.1. The cores of HCGs

Jones et al. (2023) demonstrated a noticeable difference in the deficiencies of the HCG phases, with phase 1 and 2 groups showing a similar distribution, while phase 3 groups differ notably. Although the  $\text{def}_{\text{HI}}$  distributions peak at the same values for all group phases, that of phase 3 groups exhibits a tail that extends to values an order of magnitude higher than those of the earlier phases. One of the goals of the present study is to revisit these results with deeper MeerKAT observations, for a subset of HCGs representative of the later two phases. In Fig. 8 we show a comparison between the  $\text{def}_{\text{HI}}$  values derived in this work and those of Jones et al. (2023). We note that these exclude the estimated limit values, since no estimate of the  $M_{\text{HI}}$  upper limit was given therein for non-detections. As a consequence, the majority of the objects included in the comparison are phase 2 group galaxies; the only phase 3 objects considered are HCG 90A and 97B. Since most of these masses were measured within manually drawn masks (see Sect. 4.1) which are somewhat subjective, we expect high uncertainties in the  $M_{\text{HI}}$  values. This is best seen in HCG 31 where, although the measured total HI mass of the group is higher than that reported in Jones et al. (2023) ( $1.8 \times 10^{10} M_{\odot}$  versus  $1.5 \times 10^{10} M_{\odot}$ ), our combined HI mass contained in the galaxies is lower ( $2.5 \times 10^9$  versus  $9.1 \times 10^9 M_{\odot}$ ). The remainder of the HI mass is thought to belong to the IGrM in the form of bridges and tails. Nonetheless, accounting for large uncertainties, the figure suggests a general agreement in the distributions of  $M_{\text{HI}}$ . Moreover, the scaling relation derived in this work to estimate the  $\text{def}_{\text{HI}}$  values, as well as the considered optical properties of the studied HCG galaxies, are based on recent, deep  $g$ - and  $r$ -band DECaLS photometry. However, as discussed earlier, Jones et al. (2023) made use of  $B$ -band magnitudes from Hickson et al. (1989). Two main differences are worth noting:

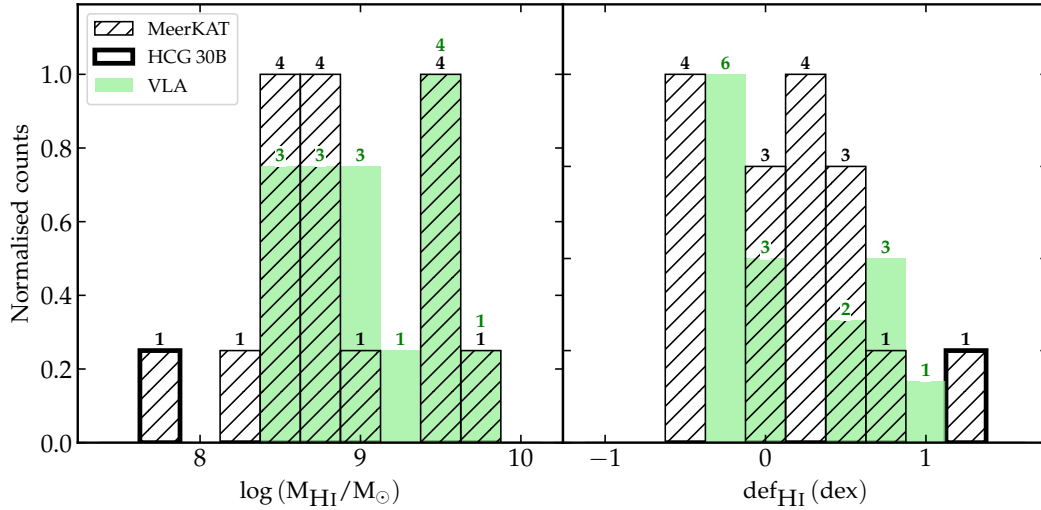


**Fig. 8.** Comparison of the distributions of the HI mass and deficiency values with the VLA measurements in Jones et al. (2023).

the different responses of the bands used, and the depths of the observations. The  $B$  magnitudes in Hickson et al. (1989) were measured out to a surface brightness of  $24.5 \text{ mag arcsec}^{-2}$ , whereas the DECaLS observations produced images as deep as  $\sim 27.9 \text{ mag arcsec}^{-2}$  (Dey et al. 2019). These differences are capable of producing discrepancies between the two measurements. Nonetheless, the mean values of the deficiencies calculated for the subsets (we remind the reader that this does not include the non-detections) are similar, with  $0.30 \pm 0.03 \text{ dex}$  for the MeerKAT measurements and  $0.31 \pm 0.03 \text{ dex}$  for the VLA results.

As was discussed in Sect. 4.2, the present MeerKAT observations allow us to set upper limits on the HI masses of the non-detections. Accounting for these limits, we note a clear distinction between intermediate and late-phase groups in the global HI deficiency of their cores, with phase 2 groups presenting ‘normal’ cores while phase 3 groups are very deficient (Fig. 7). Taken individually, the galaxies forming the cores of the groups present a similar trend in the distribution of their deficiencies, with the distribution of phase 2 galaxies peaking in the HI-normal region while that of late-phase galaxies peak in the HI-deficient region (Fig. 9). In Table 5 we present the statistics of the  $\text{def}_{\text{HI}}$  values; we note that a particular group makes an exception to the trend: HCG 31. Indeed, as many as four of the five of the group’s members are HI-poor (the fifth presents normal HI content) although its core is globally HI-normal. This is due to the HI morphology of the group: a large quantity of IGrM HI is found outside the galaxies, surpassing the combined mass of its members. A similar result was obtained in Verdes-Montenegro et al. (2005b). On the other hand, the only HI detection in HCG 97, 97B, is the only phase 3 group galaxy with an atomic gas content normal for its optical luminosity. The measured HI mass of the galaxy is  $8.7 \times 10^8 M_{\odot}$ , 82% higher than the  $4.8 \times 10^8 M_{\odot}$  VLA mass reported in Jones et al. (2023).

More generally, the median deficiency of phase 2 group members is  $\text{def}_{\text{HI},2} = 0.28 \pm 0.18 \text{ dex}$ , while that of phase 3 group galaxies (including non-detections) is  $\text{def}_{\text{HI},3} = 1.85 \pm 0.24 \text{ dex}$ . This corresponds to nearly a two-order-of-magnitude difference, indicating that during the transition from phase 2 to phase 3, the average galaxy loses almost all of its gas content. A particular example of this is seen in HCG 30. Unlike previous observations suggesting that 30B is devoid of atomic gas, the current MeerKAT campaign shows that the galaxy contains an HI

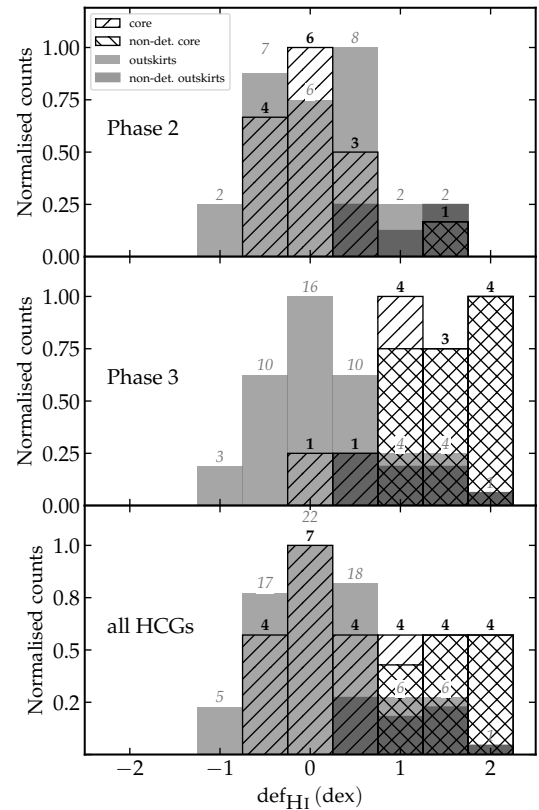


**Fig. 9.** Distribution of the HI deficiency in HCG regions for phase 2 (top), phase 3 (middle), and all (bottom) groups.

disc of measured mass  $8.1 \times 10^7 M_{\odot}$ . However, compared to its optical luminosity, the galaxy remains highly gas-deficient; in fact, it is the most HI-deficient detection of the whole sample, with  $\text{def}_{\text{HI}} = 1.4$ . In other words, 30B has lost about 96% of its atomic gas content throughout the evolution of the group. This is not surprising, given that HCG 30 constitutes the most gas-deficient of the 38 groups studied in Jones et al. (2023). Moreover, peaks of HI were also discovered at the positions of 30A and 30C, respectively. These lend support to the possibility that at least some members of the group did indeed undergo a process during which they have lost a significant fraction of their



gas content. This hypothesis is further supported by the HI morphology of HCG 90. One of the four members of the group (90A) is HI-bearing with a deficiency of 0.72 (i.e.  $\sim 80\%$  of missing HI), likely the result of a recent infall into the group (Jones et al. 2023). However, a striking feature is observed in the group: a faint filament passing through the centre of the group, with a structure similar to that connecting members of HCG 16. The column density of the gas in the filament, with peaks at  $\sim 2.6 \times 10^{19} \text{ cm}^{-2}$ , suggests that it is the remnant of a larger HI complex dissipated as a result of gas removal processes.

## 6.2. The outskirts of HCGs

The large field of view of MeerKAT ( $\sim 1^\circ$ ) enables the mapping of the targeted HCGs and their surroundings, out to  $\sim 30'$ . This advantage enables us to analyse the gas content of the groups within the context of their large-scale environment and to conduct a comparative study of their members relative to their surrounding galaxies.

As was noted in Fig. 7 and discussed in Sect. 5.2, the galaxies surrounding HCGs present a decreasing  $\text{def}_{\text{HI}}$  trend with the projected separation from the centre. Consequently, we have established that outskirts galaxies within the virial radius are  $\sim 0.3$  dex more gas-deficient than those outside. This trend is consistent with the deficiency of those observed in galaxy clusters, where the intracluster medium affects the gas content of galaxies out to  $\sim 1-2 r_{\text{vir}}$  (e.g. Giovanelli & Haynes 1985; Solanes et al. 2001; Deb et al. 2023).

In this section, we compare the outskirts to core galaxies in terms of gas content, independently of their separation from the group centre. We first consider all HCGs together, independently of their phase (bottom panel of Fig. 9), and find that they do not significantly differ from their surrounding galaxies. Although the  $\text{def}_{\text{HI}}$  histograms seem to suggest that core galaxies exhibit higher deficiencies than their surroundings, their median values are consistent within the error bars:  $0.72 \pm 0.32$  dex for core members and  $0.42 \pm 0.11$  dex for outskirts galaxies. To further verify this, we performed a Kolmogorov-Smirnov (KS) test on the cumulative distributions of  $\text{def}_{\text{HI}}$  to test the probability that the core and outskirts galaxies are drawn from the same parent population. The test provided a low degree of difference of  $k_s = 0.20$  and significance  $p = 0.36$ , well above the 0.05 significance threshold, indicating a strong similarity between the two distributions with no significant difference. This agreement between the two distributions suggests that, globally, there are no statistical differences between HCGs and their environment in terms of HI deficiency.

Next, we separate the groups by their evolutionary stage to further investigate the  $\text{def}_{\text{HI}}$  distributions (top and middle panels of Fig. 9). We note that phase 2 group galaxies exhibit deficiencies similar to their surrounding neighbours (the median  $\text{def}_{\text{HI}}$  values for core and outskirts galaxies are respectively  $0.28 \pm 0.19$  dex and  $0.29 \pm 0.23$  dex). Similarly, we performed a KS test on the two distributions, obtaining a KS statistic of 0.37 and a significance level of 0.07. This is suggestive of a moderate difference between the two distributions, although the significance is marginal. On the other hand, galaxies surrounding phase 3 groups differ significantly from the core galaxies ( $k_s = 0.65$  and  $p = 10^{-4}$ ) with deficiency values of  $0.44 \pm 0.11$  dex and  $1.85 \pm 0.25$  dex, respectively for outskirts and core galaxies.

Although, as was noted in the previous section, the galaxies in the two phases display distinct distributions, their respective surrounding neighbours show comparable HI content. As previously mentioned, the six groups were selected to best repre-

**Table 5.** Distributions of HI deficiency in galaxies in the cores and outskirts of the HCGs.

Phase	HCG	Core			Outskirts		
		% rich	% normal	% poor	% rich	% normal	% poor
2	16	60	0	40	11	11	77
	31	0	0	100	14	14	71
	91	25	50	25 <sup>(a)</sup>	45	18	36
3	30	0	0	100 <sup>(b)</sup>	57	14	28
	90	0	0	100 <sup>(b)</sup>	8	0	91
	97	0	20	80 <sup>(a)</sup>	10	34	55

**Notes.** <sup>(a)</sup>No HI detection. <sup>(b)</sup>Only 1/4 were detected in HI.

sent the HI morphologies of the two phases, including systematic variations from one phase to another. Despite their different HI deficiencies, the large-scale environments in which they evolve present similarities in the gas distributions. Based on these facts, we argue that the evolutionary stage of an HCG is independent of the large-scale environment in which it evolves, nor does it affect the HI content of galaxies outside its core. In fact, X-ray maps of HCGs in the literature (Rasmussen et al. 2008; Desjardins et al. 2013) show that when available, the hot X-ray gas in the IGrM of these groups tends to be mostly confined within their cores, rarely extending beyond the farthest group member. For example, of the six groups, only HCG 97 presents an important hot gas envelope (see Rasmussen et al. 2008). The second group with an important quantity of X-ray emission is HCG 90, whose hot gas envelope surrounds members 90B, C and D. However, as noted in Sect. 4.4.2, the hot gas is considered unlikely to spread through the group's IGrM (Desjardins et al. 2013). We argue that the notable difference of phase 3 HCGs with their surrounding is likely a consequence of the later morphological evolution of their members with respect to the rest of their environment (see, e.g. Coziol et al. 1998).

We further show in Fig. 10 the distribution of the galaxies in the plane of the sky for each HCG, colour-coded by the HI deficiency. The  $\text{def}_{\text{HI}}$  distributions do not favour a particular phase: for example, the galaxies in the regions of HCG 30 and 91 present similar distributions (see Table 5) despite the differences in the groups phases; this is also the case for HCG 31 and 97.

## 7. Summary

We have presented HI deficiencies of galaxies in and around six HCGs, selected to represent the intermediate and late phases of their evolutionary sequence. Through a MeerKAT campaign, we have aimed to update the deficiency trends observed in phase 2 and phase 3 groups from previous VLA observations (Jones et al. 2023) and study the HI content of HCGs against their immediate environment. Similarly to previous findings, we observed significant differences in the HI content of the phase 2 and 3 group galaxies. On average, phase 3 group members are  $\sim 1.5$  dex more deficient than those of phase 2. However, given the modest size of the sample and the large  $\text{def}_{\text{HI}}$  scatter among groups of the same phase, we note that this is not a general prescription for characterising the HI content of HCG members.

Mapping the HI in galaxies around the HCGs in a  $\sim 30'$  radius, we have investigated the correlation between the groups and their surrounding galaxies in terms of the  $\text{def}_{\text{HI}}$  distribution. Globally, we have found that galaxies in the cores present the same distributions as their surroundings; however, when separated by their evolutionary stage, phase 3 HCG galaxies are

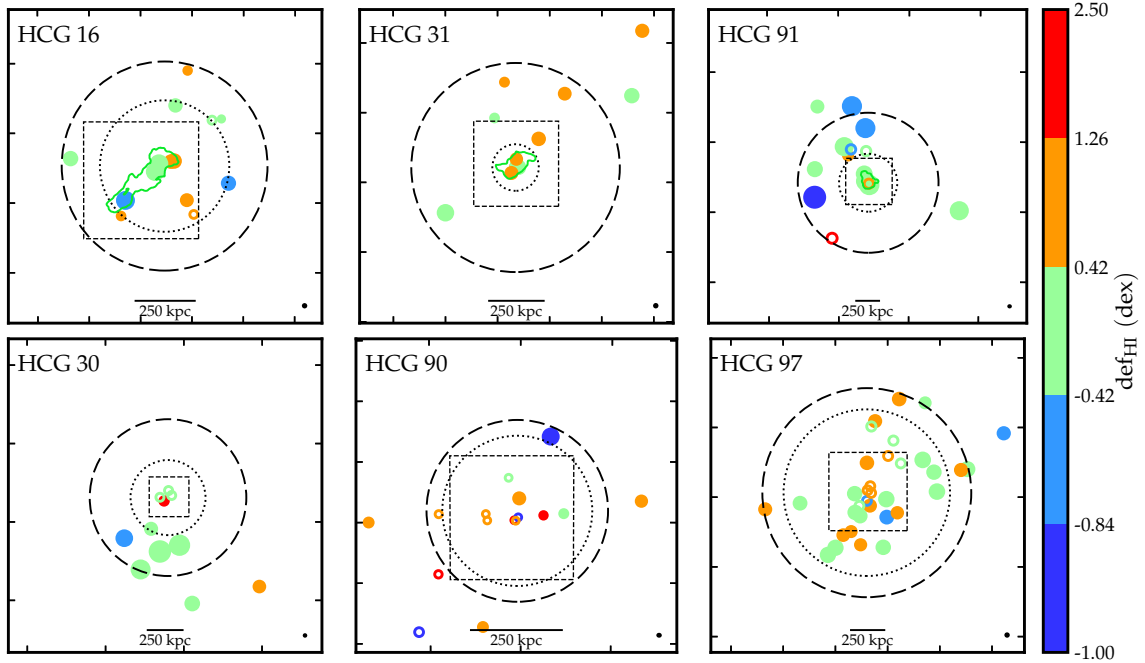


**Fig. 10.** Spatial distribution of the deficiency parameter  $\text{def}_{\text{HI}}$  in the regions of the HCGs. Circles, symbols and contour lines are the same as in Fig. 5. The size of the symbols is proportional to the HI mass. A zoomed version of this figure, highlighting the central regions, is shown in Fig. C.2.

over an order of magnitude more deficient than their outskirts. This finding supports prior studies indicating that galaxies within evolved HCGs have undergone faster evolution than the regions surrounding them.

### Data availability

All HI cubes, masks and moment maps used in this work are available in [Ianjamasimanana et al. \(2025\)](#). Additionally, the DECaLS images of the groups, the derived photometry tables of individual galaxies as well as the separated HI discs of the HCG members are available in open source in a Zenodo repository<sup>8</sup>. The repository also includes all tables and figures featured in the paper. Furthermore, in order to make the paper as reproducible as possible, we linked the Zenodo repository to a GitHub repository containing all Python scripts and Jupyter notebooks developed as part of the analysis presented in this paper. These repositories are publicly accessible.

**Acknowledgements.** The MeerKAT telescope is operated by the South African Radio Astronomy Observatory (SARAO), which is a facility of the National Research Foundation, an agency of the Department of Science and Innovation. This work used the Spanish Prototype of an SRC (SPSRC, [Garrido et al. 2021](#)) service and support funded by the Ministerio de Ciencia, Innovación y Universidades (MICIU), by the Junta de Andalucía, by the European Regional Development Funds (ERDF) and by the European Union NextGenerationEU/PRTR. The SPSRC acknowledges financial support from the Agencia Estatal de Investigación (AEI) through the “Centre of Excellence Severo Ochoa” award to the Instituto de Astrofísica de Andalucía (IAA-CSIC) (SEV-2017-0709) and together with the authors AS, LVM, RI, KMH, RGB, AdO, JP, SSE, JG, BN JM, TW and EP from the grant CEX2021-001131-S funded by MICIU/AEI/10.13039/501100011033. AS, LVM, RI, JG, SSE and TW acknowledge financial support from the grant PID2021-123930OB-C21 funded by MICIU/AEI and by ERDF/EU. RI acknowledges financial support from grant TED2021-130231B-I00 funded by MICIU/AEI and by the European Union NextGeneration EU/PRTR. BN acknowledges financial support from the grant PTA2023-023268-I funded by MICIU/AEI. TW acknowledges

financial support from the coordination of the participation in SKA-Spain, funded by MICIU. AdO and JP acknowledge further financial support from the MICIU through project PID2022-140871NB-C21 by ERDF/EU. R.G.B. acknowledges further financial support from grant PID2022-141755NB-I00. JM acknowledges financial support from grant PID2023-147883NB-C21, funded by MICIU/AEI/10.13039/501100011033. JMS acknowledges financial support from the Spanish state agency MICIU/AEI/10.13039/501100011033 and by ERDF/EU funds through research grant PID2022-140871NB-C22 and the additional support of MICIU/AEI/10.13039/501100011033 through the Centre of Excellence María de Maeztu’s award for the Institut de Ciències del Cosmos at the Universitat de Barcelona under contract CEX2019-000918-M. EA and AB acknowledge support from the Centre National d’Etudes Spatiales (CNES), France. MEC acknowledges the support of an Australian Research Council Future Fellowship (Project No. FT170100273) funded by the Australian Government. J.R. acknowledges financial support from the Spanish Ministry of Science and Innovation through the project PID2022-138896NB-C55. OMS’s research is supported by the South African Research Chairs Initiative of the Department of Science and Technology and National Research Foundation (grant No. 81737).

### References

- Abril-Pla, O., Andreani, V., Carroll, C., et al. 2023, *PeerJ Comput. Sci.*, **9**, e1516
- Alatalo, K., Appleton, P. N., Lisenfeld, U., et al. 2015, *ApJ*, **812**, 117
- Alfaro-Cuello, M., Torres-Flores, S., Carrasco, E. R., et al. 2015, *MNRAS*, **453**, 1355
- Alonso Herrero, A., García-Burillo, S., Pereira-Santaella, M., et al. 2023, *A&A*, **675**, A88
- Amram, P., Plana, H., Mendes de Oliveira, C., Balkowski, C., & Boulesteix, J. 2003, *A&A*, **402**, 865
- Amram, P., Mendes de Oliveira, C., Plana, H., et al. 2007, *A&A*, **471**, 753
- Bahé, Y. M., McCarthy, I. G., Balogh, M. L., & Font, A. S. 2013, *MNRAS*, **430**, 3017
- Barton, E., Geller, M., Ramella, M., Marzke, R. O., & da Costa, L. N. 1996, *AJ*, **112**, 871
- Blanton, M. R., Kazin, E., Muna, D., Weaver, B. A., & Price-Whelan, A. 2011, *AJ*, **142**, 31
- Blumenthal, G. R., Faber, S. M., Primack, J. R., & Rees, M. J. 1984, *Nature*, **311**, 517
- Bok, J., Skelton, R. E., Cluver, M. E., et al. 2020, *MNRAS*, **499**, 3193
- Borthakur, S., Yun, M. S., Verdes-Montenegro, L., et al. 2010, *ApJ*, **710**, 385
- Bradford, J. D., Geha, M. C., & Blanton, M. R. 2015, *ApJ*, **809**, 146
- Bradley, L., Sipőcz, B., Robitaille, T., et al. 2024, <https://doi.org/10.5281/zenodo.10967176>

<sup>8</sup> <https://doi.org/10.5281/zenodo.14965528>

- Cayatte, V., Balkowski, C., van Gorkom, J. H., & Kotanyi, C. 1990, *AJ*, **100**, 604
- Chung, A., van Gorkom, J. H., Kenney, J. D. P., & Vollmer, B. 2007, *ApJ*, **659**, L115
- Coziol, R., de Carvalho, R. R., Capelato, H. V., & Ribeiro, A. L. B. 1998, *ApJ*, **506**, 545
- Da Rocha, C., Ziegler, B. L., & de Oliveira, C. M. 2008, *MNRAS*, **388**, 1433
- de Carvalho, R. R., Ribeiro, A. L. B., Capelato, H. V., et al. 1997, *ApJS*, **110**, 1
- de Vaucouleurs, G., de Vaucouleurs, A., Corwin, H. G., Jr., et al. 1991, *Third Reference Catalogue of Bright Galaxies. Volume I: Explanations and references. Volume II: Data for galaxies between 0h and 12h. Volume III: Data for galaxies between 12h and 24h* (Springer)
- Deb, T., Verheijen, M. A. W., & van der Hulst, J. M. 2023, *A&A*, **676**, A118
- Denes, H., Kilborn, V. A., & Koribalski, B. S. 2014, *MNRAS*, **444**, 667
- Desjardins, T. D., Gallagher, S. C., Tzanavaris, P., et al. 2013, *ApJ*, **763**, 121
- Desjardins, T. D., Gallagher, S. C., Hornschemeier, A. E., et al. 2014, *ApJ*, **790**, 132
- Dey, A., Schlegel, D. J., Lang, D., et al. 2019, *AJ*, **157**, 168
- Dressler, A. 1980, *ApJ*, **236**, 351
- Džudžar, R., Kilborn, V., Murugesan, C., et al. 2019, *MNRAS*, **490**, L6
- Eigenthaler, P., Ploechinger, S., Verdugo, M., & Ziegler, B. 2015, *MNRAS*, **451**, 2793
- Espada, D., Verdes-Montenegro, L., Huchtmeier, W. K., et al. 2011, *A&A*, **532**, 117
- Gallagher, S. C., Durrell, P. R., Elmegreen, D. M., et al. 2010, *AJ*, **139**, 545
- García-Benito, R., González Delgado, R. M., Pérez, E., et al. 2019, *A&A*, **621**, A120
- Garrido, J., Darriba, L., Sánchez-Expósito, S., et al. 2021, *JATIS*, **8**, 011004
- Giovanelli, R., & Haynes, M. P. 1985, *ApJ*, **292**, 404
- Gómez-Espinoza, D. A., Torres-Flores, S., Firpo, V., et al. 2023, *MNRAS*, **522**, 2655
- González Delgado, R. M., Pérez, E., Tadhunter, C., Vilchez, J. M., & Rodríguez-Espinoza, J. M. 1997, *ApJS*, **108**, 155
- Goto, T., Yamauchi, C., Fujita, Y., et al. 2003, *MNRAS*, **346**, 601
- Gunn, J. E., & Gott, J. R. I. 1972, *ApJ*, **176**, 1
- Healy, J., Blyth, S. L., Verheijen, M. A., et al. 2021, *A&A*, **650**, A76
- Heisler, J., Tremaine, S., Bahcall, J. N., et al. 1985, *ApJ*, **298**, 8
- Herpich, F. R., Almeida-Fernandes, F., Oliveira Schwarz, G. B., et al. 2024, *A&A*, **689**, A249
- Hess, K. M., & Wilcots, E. M. 2013, *AJ*, **146**, 124
- Hess, K. M., Kotulla, R., Chen, H., et al. 2022, *A&A*, **668**, A184
- Hickson, P. 1982, *ApJ*, **255**, 382
- Hickson, P., Kindl, E., Auman, J. R., et al. 1989, *ApJS*, **70**, 687
- Hickson, P., Mendes de Oliveira, C., Huchra, J. P., & Palumbo, G. G. 1992, *ApJ*, **399**, 353
- Hu, D., Zajaček, M., Werner, N., et al. 2024, *MNRAS*, **527**, 1062
- Huchtmeier, W. K. 1997, *A&A*, **325**, 473
- Hunt, L. K., Tortora, C., Ginolfi, M., & Schneider, R. 2020, *A&A*, **643**, A180
- Ianjamasimanana, R., Verdes-Montenegro, L., Sorgho, A., et al. 2025, *A&A*, **696**, A176
- Iglesias-Paramo, J., & Vilchez, J. M. 1997, *ApJ*, **479**, 190
- Jeltema, T. E., Binder, B., & Mulchaey, J. S. 2008, *ApJ*, **679**, 1162
- Jones, M. G., Espada, D., Verdes-Montenegro, L., et al. 2018, *A&A*, **609**, 17
- Jones, M. G., Hess, K. M., Adams, E. A., & Verdes-Montenegro, L. 2020, *MNRAS*, **494**, 2090
- Jones, M. G., Verdes-Montenegro, L., Moldon, J., et al. 2023, *A&A*, **670**, A21
- Karachentseva, V. E. 1973, *Soobshch. Spets. Astrof. Obs.*, **8**, 3
- Kenney, J. D. P., Crowl, H., van Gorkom, J., & Vollmer, B. 2004, in *IAUS*, eds. P. A. Duc, J. Braine, & E. Brinks (San Francisco: Astronomical Society of the Pacific), 217, 370
- Lenkić, L., Tzanavaris, P., Gallagher, S. C., et al. 2016, *MNRAS*, **459**, 2948
- Leon, S., Verdes-Montenegro, L., Sabater, J., et al. 2008, *A&A*, **485**, 475
- Lima, E. V., Sodré, L., Bom, C. R., et al. 2022, *A&C*, **38**, 100510
- Lin, X., Wang, J., Kilborn, V., et al. 2023, *ApJ*, **956**, 148
- Lisenfeld, U., Verdes-Montenegro, L., Sulentic, J., et al. 2007, *A&A*, **462**, 507
- Lisenfeld, U., Espada, D., Verdes-Montenegro, L., et al. 2011, *A&A*, **534**, 102
- Maddox, N., Hess, K. M., Obreschkow, D., Jarvis, M. J., & Blyth, S.-L. 2015, *MNRAS*, **447**, 1610
- Makarov, D., Prugniel, P., Terekhova, N., Courtois, H., & Vauglin, I. 2014, *A&A*, **570**, A13
- Mendel, J. T., Ellison, S. L., Simard, L., Patton, D. R., & Mcconnachie, A. W. 2011, *MNRAS*, **418**, 1409
- Mendes de Oliveira, C., Plana, H., Amram, P., Bolte, M., & Boulesteix, 1998, *J. ApJ*, **507**, 691
- Mendes de Oliveira, C., Ribeiro, T., Schoenell, W., et al. 2019, *MNRAS*, **489**, 241
- Moretti, A., Serra, P., Bacchini, C., et al. 2023, *ApJ*, **955**, 153
- Ordeneš-Briceño, Y., Taylor, M. A., Puzia, T. H., et al. 2016, *MNRAS*, **463**, 1284
- O'Sullivan, E., Zezas, A., Vrtilek, J. M., et al. 2014, *ApJ*, **793**, 73
- Punzo, D., van der Hulst, J. M., Roerdink, J. B. T. M., Fillion-Robin, J. C., & Yu, L. 2017, *A&C*, **19**, 45
- Ramatsoku, M., Serra, P., Poggianti, B. M., et al. 2019, *MNRAS*, **487**, 4580
- Ramatsoku, M., Verheijen, M. A., Kraan-Korteweg, R. C., et al. 2020, *A&A*, **644**, A107
- Rasmussen, J., Ponman, T. J., Verdes-Montenegro, L., Yun, M. S., & Borthakur, S. 2008, *MNRAS*, **388**, 1245
- Ribeiro, A. L. B., de Carvalho, R. R., Coziol, R., Capelato, H. V., & Zepf, S. E. 1996, *ApJ*, **463**, L5
- Ribeiro, A. L. B., de Carvalho, R. R., Capelato, H. V., et al. 1998, *ApJ*, **497**, 72
- Rix, H.-W., Barden, M., Beckwith, S. V. W., et al. 2004, *ApJS*, **152**, 163
- Rubin, V. C., Hunter, D. A., Ford, W., Kent, J., et al. 1990, *ApJ*, **365**, 86
- Schlegel, D. J., Finkbeiner, D. P., & Davis, M. 1998, *ApJ*, **500**, 525
- Serra, P., Westmeier, T., Giese, N., et al. 2015, *MNRAS*, **448**, 1922
- Solanes, J. M., Manrique, A., García-Gómez, C., et al. 2001, *ApJ*, **548**, 97
- Solanes, J. M., Sanchis, T., Salvador-Solé, E., Giovanelli, R., & Haynes, M. P. 2002, *AJ*, **124**, 2440
- Sorgho, A., Hess, K., Carignan, C., & Oosterloo, T. A. 2017, *MNRAS*, **464**, 530
- Sorgho, A., Verdes-Montenegro, L., Hess, K. M., et al. 2024, *MNRAS*, **528**, 1630
- Springel, V., White, S. D. M., Jenkins, A., et al. 2005, *Nature*, **435**, 629
- Tovmassian, H., Plionis, M., & Torres-Papaqui, J. P. 2006, *A&A*, **456**, 839
- Turner, M. J. L., Reeves, J. N., Ponman, T. J., et al. 2000, *A&A*, **365**, L110
- Verdes-Montenegro, L., Yun, M. S., Williams, B. A., et al. 2001, *A&A*, **377**, 812
- Verdes-Montenegro, L., Sulentic, J., Lisenfeld, U., et al. 2005a, *A&A*, **436**, 443
- Verdes-Montenegro, L., Del Olmo, A., Yun, M. S., & Perea, J. 2005b, *A&A*, **430**, 443
- Vogt, F. P., Dopita, M. A., Borthakur, S., et al. 2015, *MNRAS*, **450**, 2593
- Vogt, F. P., Pérez, E., Dopita, M. A., Verdes-Montenegro, L., & Borthakur, S. 2017, *A&A*, **601**, A61
- Vollmer, B., Cayatte, V., Balkowski, C., & Duschl, W. J. 2001, *ApJ*, **561**, 708
- Wang, J., Koribalski, B. S., Jarrett, T. H., et al. 2017, *MNRAS*, **472**, 3029
- Westmeier, T., Kitaef, S., Pallot, D., et al. 2021, *MNRAS*, **506**, 3962
- White, S. D. M., & Rees, M. J. 1978, *MNRAS*, **183**, 341
- Williams, B. A., Yun, M. S., & Verdes-Montenegro, L. 2002, *AJ*, **123**, 2417
- Willmer, C. N. A. 2018, *ApJS*, **236**, 47
- Zheng, Y.-L., & Shen, S.-Y. 2021, *ApJ*, **911**, 105



## Appendix A: Tables

For readability purposes, the names of some member galaxies of Table A.3 were abbreviated following the following scheme: W=“WISEA J”, B=“APMUKS(BJ) B”, G=“GALEXASC J”, S=“2dFGRS S”, X=“2MASX J”, J=“2MASS J”. For example, W020919.28-095201.8 denotes the source WISEA J020919.28-095201.8 and G050203.46-040132.9 the source GALEXASC J050203.46-040132.9.

**Table A.1.** NED and calculated centre of mass (CoM) co-ordinates of the HCGs and their differences  $\Delta\text{pos}$ .

Phase	HCG	NED (J2000)		CoM (J2000)		$\Delta\text{pos}$ arcmin
		RA	Dec	RA	Dec	
2	16	02:09:31.32	-10:09:30.64	02:09:31.97	-10:09:25.67	0.18
	31	05:01:38.30	-04:15:25.24	05:01:39.27	-04:15:45.63	0.42
	91	22:09:10.43	-27:47:45.42	22:09:09.59	-27:47:36.70	0.24
3	30	04:36:28.61	-02:49:56.60	04:36:24.21	-02:50:42.39	1.34
	90	22:02:05.62	-31:58:00.44	22:02:04.47	-31:56:17.88	1.73
	97	23:47:22.94	-02:19:33.56	23:47:23.91	-02:18:43.08	0.88

**Table A.2.** Optical and H I properties of the HCG members.

HCG	member	$V_{\text{sys}}$ (km s <sup>-1</sup> )	Morph.	$d$ (kpc)	$g$ (mag)	$r$ (mag)	$\log M_{\star}$ ( $M_{\odot}$ )	$\log M_{\text{H I}}$ ( $M_{\odot}$ )	$\text{def}_{\text{H I}}$ (dex)	$M_{\text{H I, limit}}$
16	16A	4075.5	Sa	31.6	13.1	12.3	10.9	8.7	0.8	0
16	16B	3867.0	Sa	44.1	13.5	12.7	10.8	8.9	0.4	0
16	16C	3849.0	S0a	25.1	13.7	13.0	10.5	9.6	-0.3	0
16	16D	3874.0	S0a	44.8	13.8	13.1	10.5	9.6	-0.3	0
16	N0848	3989.0	SBab	213.1	13.7	13.2	10.2	9.6	-0.4	0
30	30A	4697.0	SBa	28.7	13.7	12.9	11.0	7.4	2.0	1
30	30B	4625.0	Sa	35.1	14.0	13.2	10.9	7.9	1.4	0
30	30C	4508.0	SBbc	48.2	15.8	15.2	9.8	7.5	1.4	1
30	30D	4794.0	S0	54.9	16.2	15.5	9.8	7.4	1.0	1
31	31A	4074.0	Sdm	3.7	14.9	14.6	9.5	8.5	0.6	0
31	31B	4136.0	Sm	13.2	15.4	15.2	9.1	8.9	0.3	0
31	31C	4037.5	Im	7.0	14.7	14.5	9.4	8.8	0.3	0
31	31G	3990.5	cI	30.2	15.0	14.8	9.3	8.6	0.5	0
31	31Q	4037.0	Im	37.4	16.9	16.5	8.9	8.5	0.7	0
90	90A	2603.0	Sa	39.9	12.7	11.9	10.8	8.6	0.7	0
90	90B	2523.0	E0	30.8	13.4	12.6	10.5	6.9	2.1	1
90	90C	2512.0	E0	20.5	13.7	12.9	10.4	6.9	2.0	1
90	90D	2775.0	Im	31.6	13.4	12.6	10.6	6.9	2.5	1
91	91A	6832.0	SBc	28.0	13.3	12.7	11.2	9.8	0.2	0
91	91B	7267.0	Sc	108.9	15.0	14.3	10.6	9.2	0.2	0
91	91C	7285.0	Sc	31.9	15.2	14.7	10.3	9.6	-0.3	0
91	91D	7195.0	SB0	13.1	14.4	13.7	10.8	7.8	1.9	1
97	97A	6932.0	E1	17.8	13.7	12.9	11.2	7.7	2.0	1
97	97B	6820.0	Sa	86.5	15.2	14.5	10.5	8.9	0.2	0
97	97C	6002.5	SBd	58.2	14.9	14.1	10.7	7.7	1.9	1
97	97D	6327.5	SBa	30.8	13.8	13.3	10.6	7.7	1.8	1
97	97E	6664.5	SB0	52.5	16.2	15.5	10.1	7.7	1.4	1

**Table A.3.** Optical and H I properties of galaxies surrounding HCGs.

HCG	member	$V_{\text{sys}}$ (km s <sup>-1</sup> )	Morph.	$d$ (kpc)	$g$ (mag)	$r$ (mag)	$\log M_{\star}$ ( $M_{\odot}$ )	$\log M_{\text{H I}}$ ( $M_{\odot}$ )	$\text{def}_{\text{H I}}$ (dex)	$M_{\text{H I, limit}}$
16	KUG 0208-103	3846.0	Sd	385.8	16.0	15.6	9.1	8.9	0.3	0
16	KUG 0206-099A	3830.0	S0	401.8	17.3	17.1	8.2	7.6	0.9	0
16	W020919.28-095201.8	3847.0	Sm	251.9	17.6	17.3	8.4	8.7	0.0	0
16	KUG 0205-104	3869.0	S0a	270.5	15.5	15.1	9.3	8.9	-0.5	0
16	KUG 0206-105	3972.0	Sc	166.6	16.2	15.9	8.9	8.6	0.6	0
16	W020825.73-095553.3	3906.0	S0	302.0	20.2	19.9	7.2	7.1	0.4	0
16	W021022.68-102345.2	4112.0	S0	271.1	19.3	18.8	7.9	7.7	0.5	0
16	W020836.71-095615.7	4026.0	Im	269.9	18.0	17.4	8.7	7.4	1.5	1
16	PGC 4584000	3163.0	S0	231.1	18.3	17.5	8.9	7.4	1.8	1

HCG	member	$V_{\text{sys}}$ (km s <sup>-1</sup> )	Morph.	$d$ (kpc)	$g$ (mag)	$r$ (mag)	logM <sub>★</sub> (M <sub>☉</sub> )	logM <sub>H I</sub> (M <sub>☉</sub> )	def <sub>H I</sub> (dex)	M <sub>H I,limit</sub>
30	NGC 1618	4888.0	SBb	332.5	13.4	12.8	10.8	10.0	-0.3	0
30	NGC 1622	4848.0	SBab	370.0	13.0	12.2	11.2	10.1	-0.4	0
30	NGC 1625	4760.5	SBb	522.4	13.5	12.8	10.9	9.8	-0.1	0
30	FGC 0495	4430.0	Scd	405.3	16.3	15.7	9.4	9.4	-0.5	0
30	MCG -01-12-037	4797.0	Sc	241.2	15.4	14.9	9.9	8.6	0.3	0
30	W043547.08-033114.6	4688.0	Sm	737.9	18.4	18.0	8.4	9.0	-0.4	0
30	W043404.12-032444.0	4588.0	Sd	865.8	17.4	17.0	8.8	8.5	0.5	0
31	W045913.48-033631.4	3630.0	Sm	824.6	15.9	15.6	9.2	8.7	0.6	0
31	W050042.68-035116.1	4033.0	E	392.5	18.8	17.9	9.1	8.6	0.7	0
31	W050300.01-042846.1	4002.0	Sm	369.1	16.7	16.5	8.7	9.3	-0.3	0
31	W050112.74-040732.1	4333.0	Sc	162.9	17.0	16.5	9.0	8.7	0.5	0
31	W045925.54-035506.3	4070.0	Sd	604.6	17.1	16.7	8.7	8.9	0.0	0
31	W050152.03-035116.1	4006.0	S0	380.9	17.9	17.5	8.4	7.8	1.0	0
31	G050203.46-040132.9	4091.0	Im	238.0	19.3	19.0	7.8	7.7	0.3	0
90	J22012971-3157464	2785.0	S0	72.0	16.7	16.1	8.8	7.6	1.6	0
90	ESO 466- G 036	2379.0	Sa	251.9	14.4	13.8	9.7	9.4	-0.8	0
90	W220250.16-325436.9	2200.0	S0	379.3	16.3	15.8	8.9	8.1	1.1	0
90	W220521.01-320000.2	2256.0	Sb	401.8	15.4	14.9	9.3	8.1	0.5	0
90	NGC 7163	2754.0	SBab	335.6	13.6	12.9	10.3	8.4	0.5	0
90	B215808.24-321139.7	2642.0	S0	125.4	17.9	17.6	7.9	7.8	0.4	0
90	ESO 466- G 046	2318.0	S0a	86.3	14.8	14.0	9.8	7.0	1.5	1
90	ESO 466- G 047	2556.0	Sbc	85.3	16.1	15.5	9.1	7.0	2.3	1
90	ESO 466- G 044	2818.0	S0	107.3	15.2	14.5	9.6	7.0	1.3	1
90	ESO 466- G 051	2632.0	S0	211.8	14.2	13.5	10.0	7.1	1.6	1
90	S408Z037	2546.0	SBc	292.3	13.7	13.1	10.0	7.2	1.9	1
90	ESO 404- G 028	2339.0	Sa	466.3	14.8	14.1	9.8	7.7	0.7	1
91	W220943.70-273554.8	7072.0	S0	372.3	18.7	18.1	8.9	8.1	1.1	0
91	ESO 467- G 016	7372.0	Sa	479.0	14.9	14.2	10.5	9.6	-0.3	0
91	ESO 467- G 014	7112.5	SBc	627.3	15.9	15.7	9.3	9.8	-0.8	0
91	ESO 467- G 003	6975.0	SBbc	1068.2	–	–	–	9.9	–	0
91	ESO 467- G 005	6868.5	Sb	974.0	15.5	15.0	10.0	9.6	-0.4	0
91	ESO 532- G 023	7235.0	SBbc	893.4	15.2	14.7	10.2	9.8	-0.5	0
91	W221035.73-271456.0	7180.0	S0	1012.7	17.0	16.6	9.2	8.6	-0.2	0
91	W221040.40-274144.2	6814.0	Sd	560.1	18.4	17.9	8.7	9.1	-0.0	0
91	W220659.01-271620.4	6931.0	Im	1140.7	–	–	–	9.0	–	0
91	W220836.49-281651.5	6966.0	Im	806.6	–	–	–	9.0	–	0
91	W220813.38-272252.5	7265.0	S0	740.6	–	–	–	8.5	–	0
91	W220913.03-273402.8	6990.5	E	363.6	15.5	14.8	10.4	7.9	1.2	1
91	W220938.70-273316.5	7435.0	E	420.1	18.9	18.5	8.4	7.9	0.8	1
91	W220727.04-275534.3	6923.0	S0	643.0	–	–	–	8.0	–	1
91	W221011.26-281122.4	7016.0	S0	732.8	15.5	14.8	10.4	8.1	1.0	1
97	W234720.25-022225.9	7247.0	S0a	94.8	17.5	17.3	8.7	8.6	0.5	0
97	LED A 1092309	7235.0	Sa	223.9	17.1	16.6	9.3	8.8	-0.5	0
97	NSA 152646	6457.0	S0	211.8	17.8	17.3	9.0	8.7	0.5	0
97	NSA 152613	6701.0	Sd	259.3	18.0	17.6	8.9	8.5	0.7	0
97	W234840.59-022144.1	6674.0	Sab	479.6	15.8	15.2	10.0	8.8	0.0	0
97	W234920.76-022329.2	7434.0	Sa	730.6	17.5	17.0	9.1	8.6	0.7	0
97	W234528.37-021158.5	6609.0	Sbc	732.9	16.4	15.9	9.6	9.0	-0.2	0
97	W234759.93-023431.4	6974.5	Sa	449.7	15.7	15.2	10.0	9.1	-0.3	0
97	W234731.71-022524.9	6223.0	Sm	172.3	17.5	17.1	9.0	8.8	0.4	0
97	UM 177	6505.0	Sc	459.8	17.3	17.0	8.9	9.2	-0.0	0
97	W234741.96-022952.2	6491.0	Sbc	297.5	18.3	17.9	8.7	8.4	0.6	0
97	W234606.83-021248.9	6626.0	Sm	498.1	17.7	17.3	8.8	8.9	0.2	0
97	W234701.65-022033.4	6767.0	Im	145.9	17.4	17.0	9.2	9.1	0.1	0
97	W234446.64-020140.0	6821.0	Sa	1059.1	17.1	16.7	9.2	8.7	-0.4	0
97	W234808.62-023634.0	6949.0	Sab	520.5	17.8	17.3	9.0	9.1	0.1	0
97	W234646.78-015151.0	6926.0	Sd	702.9	17.6	17.2	9.0	8.8	0.5	0
97	W234714.35-015813.3	6947.0	Sm	511.0	16.2	15.8	9.6	8.6	0.4	0
97	G234617.06-015255.0	7012.0	Im	759.9	19.4	19.0	8.2	8.4	0.1	0
97	W234737.41-022422.4	7051.0	Sm	162.6	18.1	17.8	8.6	8.9	-0.0	0
97	W234705.08-023423.8	7194.0	Scd	404.8	18.2	17.8	8.7	8.9	0.1	0
97	G234535.72-021211.7	7214.0	S0	687.6	17.6	17.1	9.1	8.6	0.6	0
97	W234603.39-021824.5	7171.0	Sab	497.7	17.4	17.1	8.8	9.2	-0.0	0
97	W234731.08-023340.4	7320.0	S0	372.4	18.0	17.6	8.7	8.4	0.6	0
97	W234750.99-023053.6	7364.0	Sd	344.5	18.3	17.9	8.7	8.5	0.4	0
97	MCG -01-60-040	6379.0	Sb	288.3	15.1	14.6	10.3	–	–	0
97	MCG -01-60-041	6682.0	Sa	343.0	14.0	0.3	10.9	–	–	0
97	W234732.41-022229.7	6879.0	E	107.0	19.2	18.5	8.9	7.7	1.4	1

HCG	member	$V_{\text{sys}}$ (km s <sup>-1</sup> )	Morph.	$d$ (kpc)	$g$ (mag)	$r$ (mag)	$\log M_{\star}$ ( $M_{\odot}$ )	$\log M_{\text{HI}}$ ( $M_{\odot}$ )	$\text{def}_{\text{HI}}$ (dex)	$M_{\text{HI,limit}}$
97	W234659.42-020811.6	6459.0	S0	301.1	17.1	16.4	9.7	7.8	0.6	1
97	X23464481-0210169	6894.0	E	318.3	15.9	15.0	10.5	7.8	1.1	1
97	2MFGC 17840	6447.0	S0	415.0	16.9	16.1	9.8	7.8	0.7	1
97	W234718.75-015943.3	6853.0	E	470.8	16.0	15.3	10.2	7.8	1.0	1

## Appendix B: Impacts of classifying ESO 466-G044/46 as HCG 90 core members

The systematic search for HCG members in Sect. 3.3 has identified two galaxies, ESO 466-G044 and ESO 466-G046, as potential members of HCG 90. However, given that the galaxies present no apparent sign of interaction with the group, we have opted to not include them in the late-phase group. In this section, we present the alternate scenario of accounting these galaxies in the core. Specifically, we verify its impact on the main results of the analysis, contained in Fig. B.1.

A comparison of the figure with Fig. 9 shows no notable differences. Specifically, the deficiency distribution of phase 3 groups is still distinct from that of the surrounding galaxies ( $k_s=0.69$  and  $p=10^{-5}$ ), with respective median values of  $1.52 \pm 0.22$  dex and  $0.42 \pm 0.12$  dex. Moreover, the core galaxies of the total sample (combined phase 2 and 3 groups) present a median deficiency parameter of  $0.76 \pm 0.35$  dex while the surrounding galaxies exhibit  $0.41 \pm 0.12$  dex.

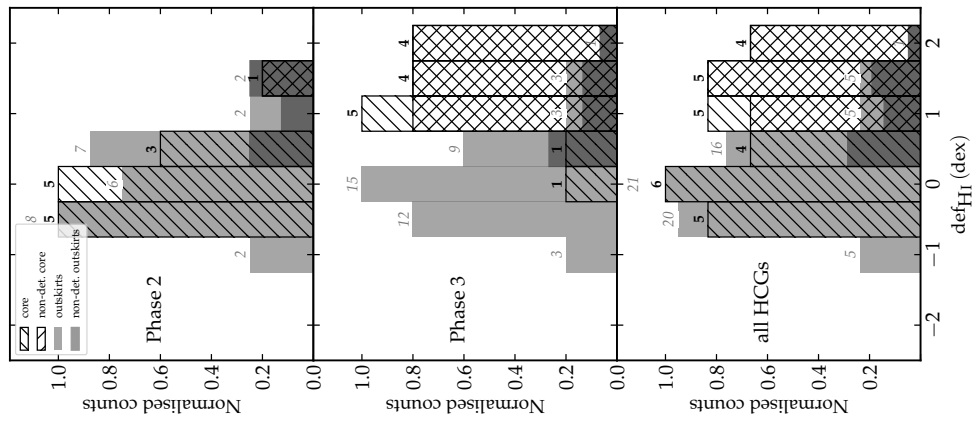


**Fig. B.1.** Same as Fig. 9 but with galaxies ESO 466-G044 and ESO 466-G046 considered as core members of HCG 90.

## Appendix C: Posterior distribution and zoom-in on the cores



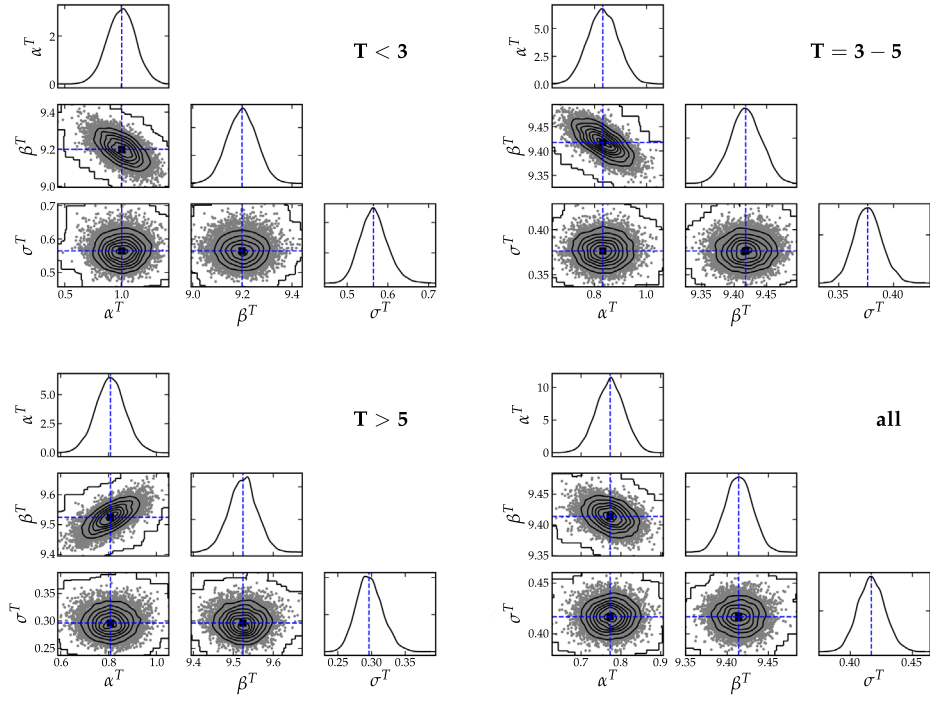


**Fig. C.1.** The posterior distributions of the regression parameters for the AMIGA galaxies and for each of the morphological bins.

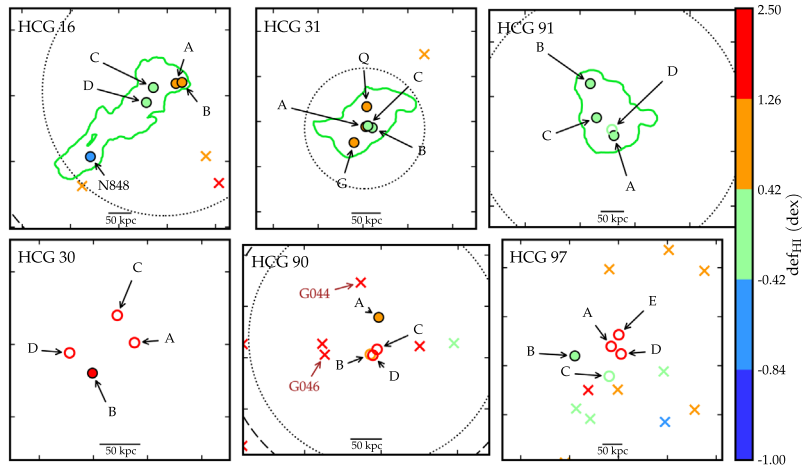


**Fig. C.2.** Central regions of Fig. 10. The core galaxies are labelled with letters and outskirts galaxies are marked with crosses.